QATAR UNIVERSITY

COLLEGE OF ARTS AND SCIENCES

PREPARATION AND CHARACTERIZATION OF FLEXIBLE ALL SOLID STATE CNTS/MNO2 SUPERCAPACITORS

BY

HANAA DAWOUD

A Thesis Submitted to the Faculty of

the College of Arts and Sciences

in Partial Fulfillment

of the Requirements

for the Degree of

Masters of Science

in

Material Science and Technology

June 2018

© 2018 Hanaa Dawoud. All Rights Reserved.

COMMITTEE PAGE

The members of the Committee approve the Thesis of Hanaa Dawoud

defended on 20/05/2018.

_____

Prof. Talal Altahtamouni
Thesis/Dissertation Supervisor

_____

Prof. Nasr Bensalah
Thesis/Dissertation Co-Supervisor

_____

Prof. Aboubakr Ali
Committee Member

_____

Dr. Khaled Saoud
Committee Member

Approved:

_____

Rashid Al-Kuwari, Dean, College of College of Arts and Sciences

ABSTRACT

DAWOUD, HANAA, DAWOUD., Masters : June : 2018, Material Science and Technology

Title: Preparation and characterization of flexible all solid state CNT/MnO_2 Supercapacitors

Supervisor of Thesis: Prof. Talal, M., Altahtamouni.

In this work, CNTs/MnO_2 hybrid supercapacitors were prepared using RF magnetron sputtering as deposition technique. The as-prepared composite materials were characterized by different morphology and spectroscopy techniques, CNTs/MnO_2 composites were then tested as electrode materials in symmetric supercapacitors in solution and in solid state.

The surface morphology, structural and mechanical properties of the CNTs and CNTs/MnO_2 electrodes were characterized by Raman spectroscopy, scanning electron microscope-energy dispersive spectroscopy (SEM-EDS), X-ray photoelectron spectroscopy (XPS), and X-ray diffraction (XRD). XRD, Raman spectroscopy and XPS measurements confirmed the formation of MnO_2 films. While SEM images demonstrated, the uniform distribution of MnO_2 layers. Furthermore, tensile tests demonstrated the flexibility of the prepared CNTs/MnO_2 composite electrodes.

The electrochemical behavior of three CNTs/MnO_2 composites with 350, 700, and 1000 nm thick MnO_2 was investigated in 1 M Na_2SO_4 aqueous solution via cyclic voltammetry (CV), electrochemical impedance spectroscopy (EIS), and galvanostatic charge/discharge (GCD). The CV and GCD tests showed that all electrodes with different MnO_2 thicknesses exhibit excellent pseudocapacitive behavior as compared with CNTs sheet in the potential window of 0 -1.0 V for CV and 0 - 0.8 V for GCD.

At small scan rates (5 mV/s), the electrode of 1000 nm MnO_2 thickness displayed specific capacitance of CV (1676 F/g), which is much higher than that of the other electrodes (609, and 441 F/g) for the electrodes with 700 nm and 350 nm, respectively. The specific capacitance measured using charge/discharge process showed similar thickness dependence as in CV measurements, where the specific capacitance increases with increasing the MnO_2 thickness.

Additionally, the electrode with 1000 nm MnO_2 thickness exhibited a cyclic stability with capacitance retention of 85.8% of its peak value after 400 cycles meanwhile, the other electrodes exhibited almost the same cyclic stability with capacitance retention of 59% after 400 cycles.

The all solid-state flexible supercapacitors consisting of two-electrode system with a PVA/H_3PO_4/CNTs/MnO_2 symmetric capacitor with 1000 nm MnO_2 thickness showed the highest specific capacitance in comparison with the other devices with 350 and 700 nm thick MnO_2. The device with 700 nm thick MnO_2 exhibited the best cyclic stability with capacitance retention of 67% of its initial capacitance after 400 cycles compared with the other devices.

DEDICATION

This thesis is dedicated to my family who have always been a constant source of support and encouragement during the challenges of my whole life. Also to my friends who were the source of support, and power all through the journey towards achieving the best I can do.

ACKNOWLEDGMENTS

There is a number of people without whom this thesis might not have been written, and to whom I am greatly indebted.

I would like to express my sincere gratitude to Prof. Talal Altahtamouni, my thesis supervisor who gave me the golden opportunity to do my thesis project with him and for his encouragement in carrying out this project.

I sincerely thank Prof. Nasr Bensalah, my co-supervisor for providing me all the needed information with continuous support and guidance towards the completion of this project.

I am very grateful for the faculty members of the Material sciences and Technology Program, Dr. Talal M. Al-Tahtamouni, Dr. Khaled M. Youssef, Dr. Ahmed Elzatahry and Dr. Abou bakr for their valuable help and for giving me the chance to join the program.

Furthermore, Special thanks to the staff of the Central Laboratory Unit (CLU) and the Center for Advanced Materials (CAM) for giving the access to their facilities.

Finally, I would like to thank all my colleagues, researchers, and post-doctors for all the positive vibes and continuous support and encouragement. Last but not least, I am grateful to my parents Dawoud and Intesar and sister Heba for their patience, love, and unconditional support.

TABLE OF CONTENTS

LIST OF FIGURES

CHAPTER 1: INTRODUCTION

With the massive revolution of the global economy and the increase in the energy consumption, the demand for more energy sources, energy conversion and storage with high efficiency, environment-friendly, and sustainable becomes significant. Currently, the production of energy storage systems such as solar panels batteries and electrochemical supercapacitors (ES) is moved to more productive solutions to reach the highest sufficiency. Even though batteries dominate the energy storage market, they have low power density, low rate and a small number of charge-discharge cycles. These obstacles can be overcome using supercapacitors. Supercapacitors or known as ultracapacitors have attracted great attention for advanced energy storage due to their high power and energy densities[1], high capability, long lifecycle and high charge-discharge rates.[2]

There are two categories of supercapacitors depending on their charge storage mechanisms, electrical double-layer capacitors (EDLCs) and pseudocapacitors. In EDLCs the capacitance results from the charge separation at the electrolyte and electrode interface. In pseudocapacitors capacitance results from the reversible Faradaic reaction at the electrode surface. This indicates the importance of the electrode material in determining the efficiency and the capacitance of supercapacitors. In EDLCs carbon allotropes are the most commonly used electrode material; activated carbon (AC)[3,4], graphene[5–7], carbon nanofibers[8,9], and carbon nanotubes (CNTs)[10,11]. Transition metal oxides and conducting polymers are used as pseudocapacitor electrode materials.[12]

1.1 Types of Supercapacitors

There are three classifications of supercapacitors based on the charge storing mechanism such as electrochemical, electrostatic and hybrid as shown in Figure 1.

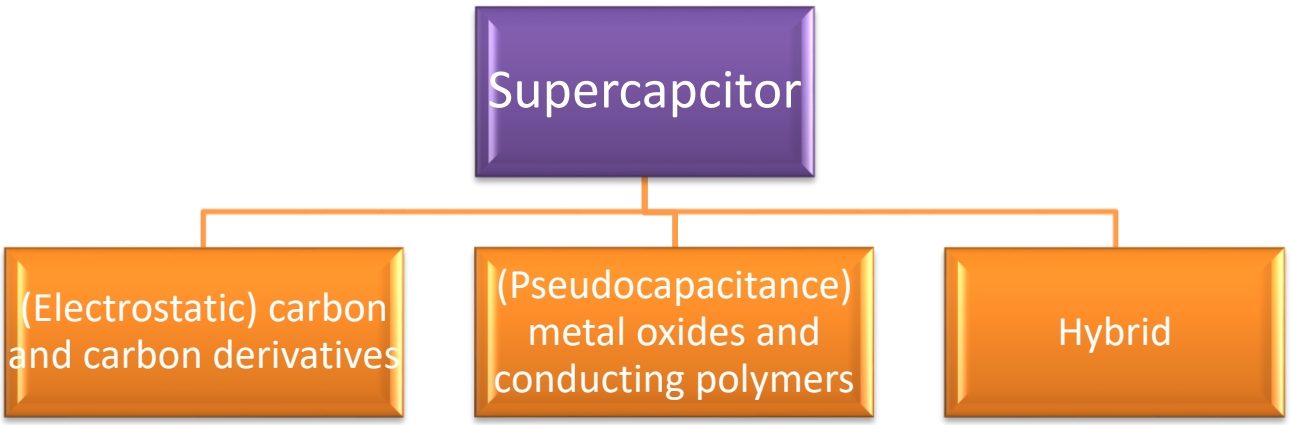

Figure 1: The classification of Supercapacitors

1.1.1 Electrostatic capacitors (EDLC)

In general, the electrostatic capacitor is referred as EDLC which derived from the principle of storing the electrostatic charges in the electric double layer of supercapacitor

at the electrode-electrolyte interface.[13,14] EDLC consists of three main parts electrode, electrolyte, and the separator. The distance of separation between the electrodes in conventional capacitors (in micrometer scale) is relatively bigger than the thickness of the double layer (in angstrom scale). The charges then stored in the interface between the electrolyte and the conductive carbon particles. The capacitance of EDLC can be measured by the equation[15]:

$$C_{dl}=\frac{(1\varepsilon)(2\varepsilon)A}{d} \quad (1)$$

Where C_{dl} is the capacitance of EDLC, 1ε is the relative dielectric constant, 2ε is the permittivity of free space, *A* is the surface area of the electrode in the double layer and *d* is the thickness of the double layer.

Carbon or its derivatives like carbon aerogel, carbon nanotube (CNTs) and graphene are the most used as electrode materials for EDLC. It's worth mentioning that the porous nature of carbon material delivers large surface area and reveal high conductivity. Carbon nanotubes (CNTs) have attracted much attention from different corners because of their useful thermal[16], mechanical[17], and electrical[18] properties. In 1991, carbon nanotubes (CNTs) was discovered for its first time by Iijama [19]. The researchers investigated CNTs in their work mainly in synthesizing the electrodes of supercapacitors because of its properties like high surface area, excellent cycling stability, low specific capacitance, superior rate capability and low energy density[11] which in turn enhances the excellence of supercapacitors by improving the chemical stability, mechanical strength, and electrical properties.[20] To improve the properties of CNTs based supercapacitors, conductive polymers or metallic oxides are added to CNTs electrodes.

The electrolyte is used to define the operating potential as well as to offer for ion conduction. Selection of the electrolyte is based on the type of electrode material, cost, the pore size and other parameters. The separator works as a barrier to avoid any electron or electrical contact between the supercapacitor electrode. Nonetheless, the ions can pass through the separator.

The mechanism of electrostatic supercapacitor is based on forming an electrical double layer at the surface which is produced from the particles of electrode material at the interface between the metal oxide particles for example (RuO, MnO_2 or ZnO) and electrolyte, where the overabundant electric charges are stored on the surfaces of the electrode, and also with the electrolyte ions with counterbalancing charge are built from the electrolyte side for to reach the electroneutrality. Through charging process, the electrons move from cathode (negative electrode) to the anode (positive electrode) over an external load. On the other hand, anions travel to the positive electrode through the electrolyte, while cations go from the positive electrode toward the negative electrode. However, the reverse process occurs in the discharge process. In electrostatic supercapacitor, there is no transfer of the charge across the electrode/electrolyte interface, besides no net ion exchanges, take place between the electrode and the electrolyte. This indicates that the concentration of electrolyte stays constant through the charging/discharging processes and the energy is stored in the double-layer interface. Figure 2 displays the structure and mechanism of EDLC.

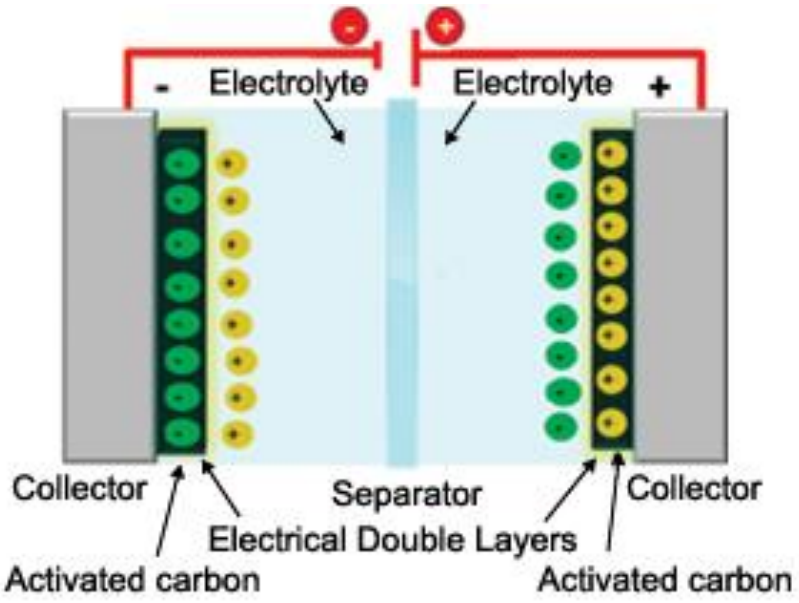

Figure 2. Structure of supercapacitor (EDLC)

1.1.2 Pseudocapacitors

On the contrary, pseudocapacitors can store electrical energy on the surface of the electrode by oxidation and reduction reactions.[2,21,22] The energy density enhanced by the faradaic process that supports the energy stored in a pseudocapacitor, however, the efficiency of power density and cycle life faded compared to EDLCs.[21] Pseudocapacitors electrode is mainly transition metal oxides (e.g. Co_3O_4,[23,24] MnO_2,[25,26] and RuO_2[27–29] etc.) and conducting polymers,[30–33] they are receiving particular attention owing to their high

theoretical capacitance and natural abundance.[34] Furthermore, a high surface area with micro-pores supports the ion access to the electrode material.[35] The capacitance of pseudo-capacitance can be found by the equation [36]:

$$C = \frac{Q}{V} \tag{2}$$

Where C is the capacitance of pseudocapacitance, Q is the total charge of the electrode and V is the voltage change for a charge or discharge. Pseudo-capacitors showed a capacitance range from 10 to 100 times higher than that of a carbon double layer capacitor.[36] Figure 3 presents the Faradaic charge-transfer by display the double-layer adsorbed ions that transfer their charges to the electrode.

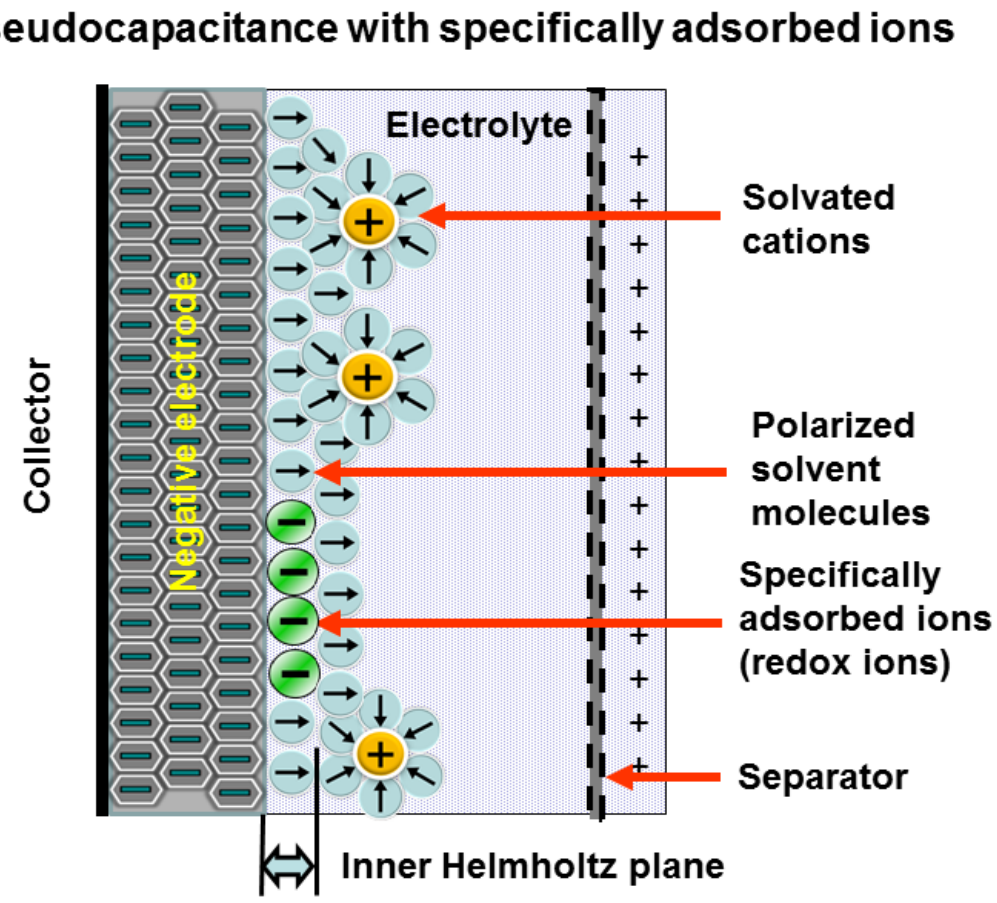

Figure 3. A simplified view of a double-layer with specifically adsorbed ions which have transferred their charge to the electrode to explain the faradaic charge-transfer of the pseudocapacitance.

Among the several pseudocapacitive transition metal oxides materials, manganese dioxide (MnO_2) has displayed many interesting properties for its natural abundance, excellent electrochemical capacitive properties, environmental friendliness, wide potential

range, low cost,[37,38] and high theoretical specific capacitance 1370 F/g.[39] The pseudocapacitive reaction of MnO_2 considers as a surface dominant reaction, only the surface of the electrode or a very thin surface layer of the oxide can participate in this pseudocapacitive reaction. Despite, MnO_2 suffers from poor ionic and electrical conductivity (10^{-5}–10^{-6} S/cm) which limits achieving the high theoretical capacitance for supercapacitors.[40] The microstructure and surface area of MnO_2 compounds play a major role in its electrochemical behavior. So, the enhanced fabrication methods should provide well-constructed nano-sized particles with higher active materials area.

1.1.3 Hybrid Supercapacitors

To reach higher improvements; advanced methods were used to enhance the EDLS capacitance and pseudocapacitors conductivity, by hybridizing both of the electrode material Faradaic and non-Faradaic supercapacitors.[41,42] Hybrid supercapacitors are categorized into three types composites, redox asymmetric and batteries-like as shown in figure 4. Hybrid supercapacitors are expected to increase the merits and reduce the demerits that exist in both EDLCs and pseudocapacitors. It has been proven that hybrid double-layer supercapacitors can reach greater energy density, better cyclic stability in addition to higher specific capacitance compared to EDLS and pseudocapacitors.[41] A composite film of graphene oxide maintained by needle-like MnO_2 nanocrystals presented excellent electrochemical performance compared to that of only using MnO_2.[43] A rational design of ternary nanocomposite composed of CNTs, MnO_2, with conducting polymer revealed great electrochemical performance as a result of the effective employment of all the desired functions of each component.[44]

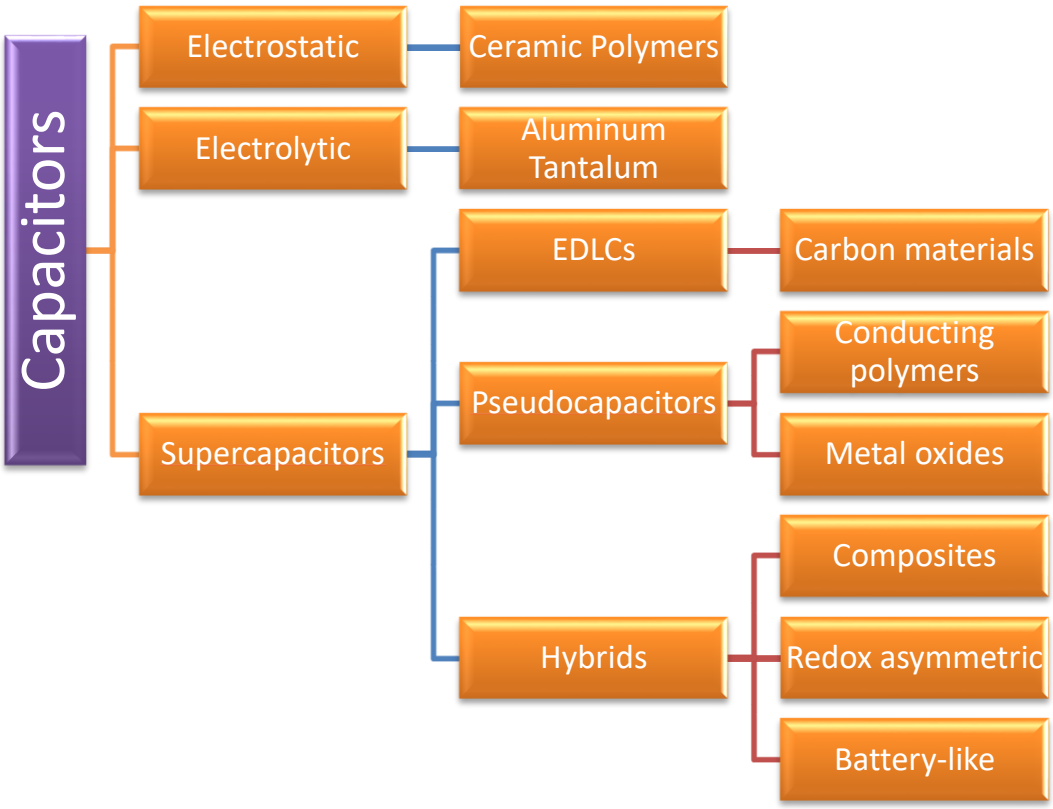

Figure 4. classification of capacitors

Various synthesis methods have been used to coat a thin film of MnO_2 on the surface of CNTs nanostructures substrates, for instance, co-precipitation[39], sol-gel[45], chemical redox deposition[46] and electrodeposition[47] techniques have been studied widely. Although chemical techniques used to fabricate metal oxide nanostructured exhibit toxic solvents and reagents. Also, the usage of binders and additive during these techniques leads

to combining them with the active materials which reduce the supercapacitor capacitance.[48] The physical approach shows an environment-friendly way to produce contamination free metal oxide nanostructured materials. Physical vapor deposition (PVD) approach especially sputtering presents a successful method to synthesize high quality, binder free and eco-friendly nanostructures supercapacitor electrodes.[49]

In this work, we introduce a strategy to produce flexible CNT/MnO_2 hybrid film. For the first time, RF magnetron sputtering technique used to grow a thin film of MnO_2 on CNT sheet at three different thicknesses (350 nm, 700 nm, and 1µm). The obtained sheet is utilized as a working electrode to improve the performance of supercapacitors. The electrode synthesis is done in two steps, CNTs sheet produced via floating catalyst chemical vapor deposition (CVD). Followed by deposition of MnO_2 on CNTs sheet by RF magnetron sputtering. The significant aspect of sputtered MnO_2 material is that it binds directly to CNTs current collector without any binder's requirement. In this case, the specific capacitance is increased with great stability over long cycling.[50] The effect of MnO_2 thickness on the electrochemical and mechanical properties of CNTs/MnO_2 hybrid material is evaluated. In addition, all solid state symmetric CNT/MnO_2 supercapacitors are fabricated using polyvinyl alcohol PVA-H_3PO_4 gel as the electrolyte.

Objectives

- To deposit MnO_2 layer on CNTs sheet using RF magnetron sputtering technique.
- To study the effects of MnO_2 thickness on supercapacitor application.
- To Study the performance and stability of the composites for supercapacitor application.

- To produce full supercapacitor device and study the performance.

CHAPTER 2: LITERATURE REVIEW

Electrochemical supercapacitors achieved the novel applications in different energy storage devices, for instance, electric and hybrid vehicles and aircraft.[51,52] Finding the highest specific capacitance as well as energy density in the electrodes with high active mass loading is the main goal for the researchers to go with further discoveries by using various active materials like carbons derivatives and transition metal oxides. It has been demonstrated that MnO_2 is one of the most encouraging materials for charge storage due to its high theoretical specific capacitance of 1400 $F.g^{-1}$ in a comparatively large voltage window.[53] Though, due to poor electrolyte access to the material surface and the low electronic conductivity of MnO_2, the specific capacitance reduced drastically with increasing the load of the active mass, chiefly at high charge-discharge rates.[54–56] Researchers successfully combined CNT and pure MnO_2 into a composite of MnO_2/CNT.[57–63] In this chapter, the results and issues of available works in the literature on using CNTs coated with MnO_2 electrode materials for supercapacitors are presented.

Chemical redox deposition

Generally, to achieve redox deposition of metal oxides, a strong-oxidant precursor such as FeO_4^{2-}, MnO_4^- or RuO_4 are used and reacting at the surface of carbon (performing as reductant), which features of scalability, cost, and manufacturability.[55] Lee, T., and co-authors (2018) improved the stability of asymmetric supercapacitors and studied the high energy and power densities via producing nanodot MoO_3/CNT and mesoporous MnO_2/CNT free-standing films. Asymmetric supercapacitors synthesized by two different electrode materials were both displayed pseudocapacitance type with great voltage window

of 2 V. Hence, the specific surface area enhanced to 343 m^2/g and 68 m^2/g for MoO_3/CNT. Moreover, the conductivity improved to 2.27 for MoO_3/CNT and 10.82 F/cm for MnO_2/CNT. Furthermore, asymmetric supercapacitors prepared with Na_2SO_4 as the electrolyte revealed a great energy density of 27.8 Wh/kg and power density 9.8 Wh/kg at a high power density of 10,000 W/kg. Additionally, the ASC demonstrated superb cycle stability with a capacitance loss of 3.2% after 10,000 cycles at 5 A/g.[64]

Patil, B. et al. (2018) studied the lightweight, stackable all-solid-state supercapacitors based on MnO_2 material combined with highly conductive 3D-networked CNT web paper. By using the chemical technique to deposit a layer of MnO_2 on CNT-web paper and depicted a specific areal capacitance at 5 mV/s reached to 135 $mF.cm^{-2}$ with a capacitance fading of only 5% after 10,000 cycles. Thereafter, asymmetric solid-state supercapacitor synthesized by two electrodes of web paper of MnO_2/CNT that exhibited a high areal capacitance of 57 mF/cm^2 with an energy density of 0.018 mWh/cm^2 and a capacitance loss of 14% after 10,000 cycles. [65]

Jin E. et al. (2017)[46] synthesized composites of CNT/MnO_2 by using chemical redox deposition to enhance the electrochemical pseudocapacitor properties and to improve the electrical conductivity, the composites were wrapped in functionalized graphene nanosheets (fGNSs) as shown in Figure 5. Furthermore, this method led to the reduction of MnO_2 loss during the charge-discharge process. After studying the electrochemical properties using a three-electrode system, they found that the CNT/MnO_2 electrode deposited for one hour presented the highest specific capacitance around 180 F/g, with only 10% loss of a discharge capacity. While the results presented in Figure 6 of the composite fGNS-CNT/MnO_2 electrode deposited at the same time (1 h) showed 202 F/g and a great

cycling stability of 95%. In addition, using the two-electrode system for producing an asymmetric capacitor with an activated carbon//fGNS-CNT/MnO_2 asymmetric capacitor, they found that the initial capacitance was reduced by only 5% after 1000 cycles, and the corresponding energy densities and power were calculated at 8 mA cm^{-2} to be 46 W h kg^{-1} and 720 W kg^{-1} respectively.

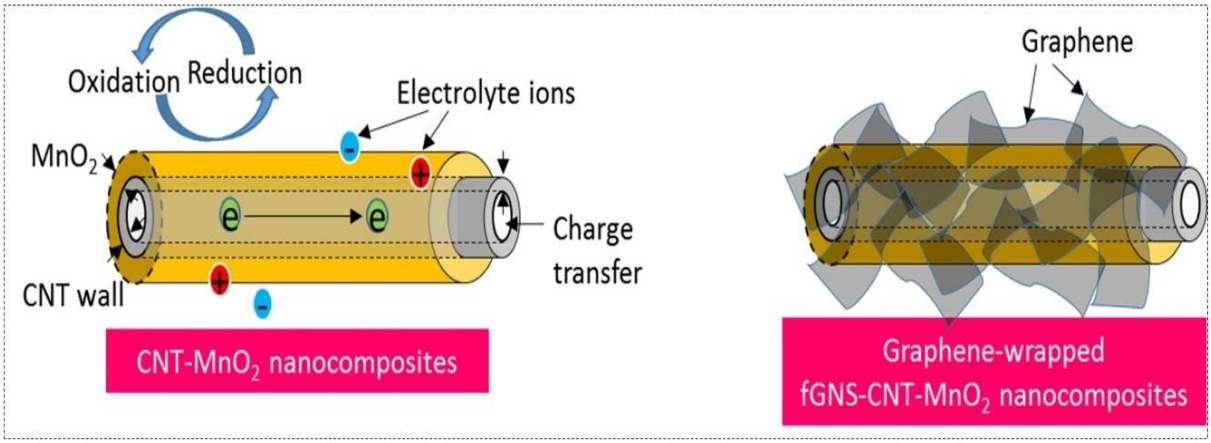

Figure 5. Schematic illustration of CNTs-MnO_2 and graphene-wrapped fGNS-CNTs-MnO_2 nanocomposites.[46]

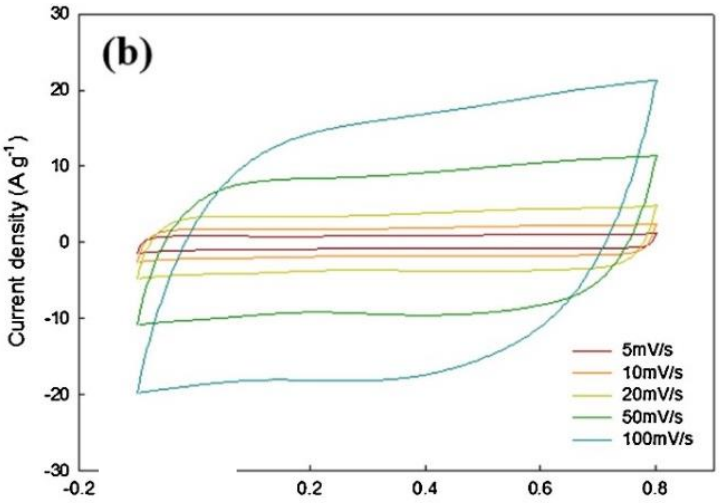

Figure 6. CV curves of CNT-MnO_2 (1.0 h) electrode used supercapacitor at different scan rates.[46]

Qi, W. et al. (2017) MnO_2 nanosheets were deposited on top of the CNTs paper by using a self-controlled redox method in $KMnO_4$ solution. Then the composite was fabricated as supercapacitor electrodes without using conductive agents or any binder. The composite film presented area specific capacitance of 1980 F/m^2 with great capacitance retention of 87% after 3000 cycles at 10 A/m^2. On the other hand, the symmetric supercapacitor maintained an energy density of 177 Wh/m^2 at a power density of 250 W/m^2.[66] Chodankar, N., Ji, S. and Kim, D. (2017) studied the asymmetric solid-state supercapacitors via establishing of MnO_2/MWCNTs nanocomposite loaded on a stainless-

steel mesh substrate. A chemical method; potentio-dynamic electrodeposition was used to enhance the capacitive properties of MnO_2 based electrodes. The prepared MnO_2/MWCNTs nanocomposite revealed a high specific capacitance of 614 F/g and a high specific energy of 85.3 Wh/kg. After assembling the MnO_2/MWCNTs nanocomposite electrode for asymmetric solid-state supercapacitor and using polyvinyl alcohol (PVA)/Na_2SO_4 gel electrolyte, the cell successfully obtained a great specific capacitance of 204 F/g with an energy density of 28.33 Wh/kg. Furthermore, the capacitance decreased by only 0.96%.[67] Gueon, D. and Moon, J. (2017) introduced high-performance supercapacitors using MnO_2 nanoflake/CNT core-shell particles. MnO_2/CNT core−shell particles were prepared with different thicknesses of MnO_2 layers and are used to study the electrochemical performance and successfully reached a specific capacitance of 370 F/g at 0.5 A/g current density with only 85% of MnO_2/CNT core−shell particles upon their supercapacitor electrode application. Besides that, an asymmetric capacitor based on the CNT/MnO_2 particle is assembled and exhibited a high power density of 225 W/kg and an energy density of 27 Wh/kg. [68] Zhao, Y. co-authors (2017) reported the compressible graphene/CNT/MnO_2 aerogel as the electrodes of SCs.[69] They found the specific capacitance of 106 F/g. However, after measuring the compressive strains of the aerogel, it was found that recoverable compressive strains are an excessively low strain (50%) which resulted by the week attachment of MnO_2 particles on graphene/CNT scaffold. Huang, H. et al. (2015) used direct redox route to synthesize nanostructured MnO_2 on carbon nanotubes (CNTs). Moreover, the reaction time was changed to monitor the growth density of MnO_2 beside the structural integrity of CNTs. As a consequence, the prepared MnO_2/CNT electrodes displayed an excellent specific capacitance of 247.9 F/g, with

excellent cycling stability of 92.8% retention after 5000 cycles, suggesting for this electrode to be a potential modest contender in the application of supercapacitor.[70] Likewise, in 2011, Wang, H. et al. combined MnO_2/CNT via a facile direct redox reaction. After 2000 cycles, the composite with content 44.4% of MnO_2 displayed a specific capacitance of 119.3 F/g and 90% of its specific capacitance was remaining.[71] Wang, H. et al. (2013) designed carbon-coated carbon nanotubes (C@CNT) and employed them as a conductive electrode to synthesis MnO_2/C@CNT composite. The use of C@CNT with self-sacrificial carbon sheet as a preservation enables loading higher amount of MnO_2. They were able to produce a MnO_2/C@CNT composite with 78 wt% MnO_2. At a current density of 0.2 A/g, the electrochemical behavior of MnO_2/C@CNT composite showed a high specific capacitance of 227 F/g. In addition, after 1000 CV scans, the stability was high with only 6% decay of its maximal specific capacitance. Figure 7 shows the curves of cyclic voltammetry and galvanostatic charge/discharge of MnO_2/C@CNT. [38]

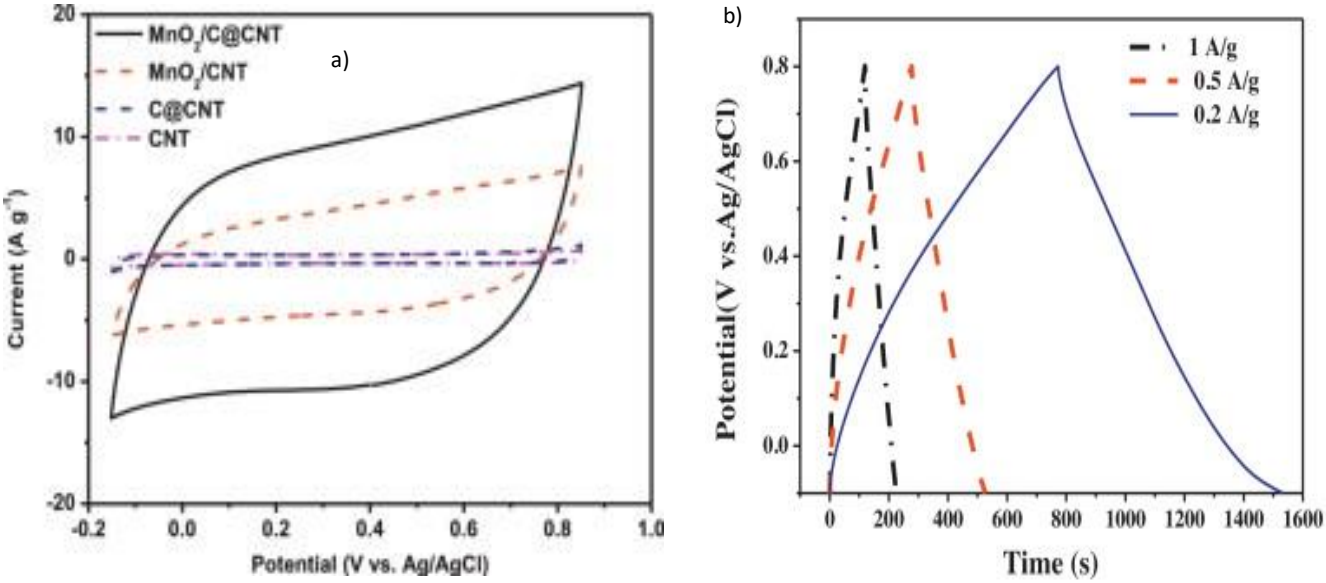

Figure 7. The curves of (a CV for CNT, C@CNT, MnO_2/CNT and MnO_2/C@CNT (b) CGD of MnO_2/C@CNT at various current densities. [38]

Hu, L. et al. (2011)[72] reported the electrodeposition of MnO_2 nanoflowers on CNT enabled conductive textile fibers. The composite with a large mass loading of 8.3 mg/cm^2, showed an areal capacitance of 2.8 F/cm^2 and high specific capacitance of 410 F/g at 0.05 mV/s. In 2007, Jin, X. et al. prepared nanocrystalline MnO_2 to cultivate in the cavity of CNTs and on the surface. Moreover, it has been found that the CNT/MnO_2 offered a specific capacitance of 144 F/g with the amount of 65 wt % MnO_2 sample.[73] Lee, S. et al. (2010) investigated MWNTs/MnO_2 nanocomposite ultrathin film using redox deposition of MnO_2 on layer-by-layer (LbL) accumulated MWNTs films. The electrodes LbL-

MWNT/MnO_2 revealed a high volumetric capacitance with great capacity retention reaching 246 F/cm^3 up to 1000 mV/s. This was due to rapid transport of ions and electrons within the electrodes.[74] Chou et al. (2008) CNT sheet was coated with MnO_2 nanowires via a cyclic voltammetric method. This composite showed a specific capacitance of 107.9 F/g. In conclusion, 19.8% of MnO_2 was deposited on the electrode and it was less than 12% of the initial capacitance after 3000 cycles.[75]

In-situ process

In situ process in electrochemistry depends on performing electrochemical experiments under operating states of the electrochemical cell such as under specific potential control.

Potential control maintains the electrochemical environment to preserve the double layer structure as well as the electron transfer reactions occurring at that certain potential in the electrode/electrolyte interfacial region.[76,77] Akbulut, S. et al. (2017) presented the production of 3D nanostructured supercapacitor micro-electrode arrays by utilizing MnO_2/CNTs composite on graphite foil substrate. Also for integrating a solid-state supercapacitor cell, PVA/H_3PO_4 solid polymer electrolyte used. The current conductor, which is the 3D CNT microelectrode arrays was synthesized by hot filament chemical vapor deposition (HFCVD) method. While an electrochemical technique; in-situ reduction of $KMnO_4$ was used to achieve the thin-film MnO_2 deposition on the CNTs. For the electrochemical characterization, KCL aqueous electrolyte used and exhibited a specific capacitance of 858 $F \cdot g^{-1}$ at a scan rate of 1 $mV \cdot s^{-1}$. Asymmetric solid-state supercapacitor cell assembled and obtained a specific capacitance round 830 $F.g^{-1}$ at 1$mV \cdot s^{-1}$. The high specific energy of 115.2 $Wh.kg^{-1}$ and specific power of 73.9 $kW \cdot kg^{-1}$ were achieved. Also,

it showed excellent cycling stability of 89% with a capacitance retention after 3000 cycles.[78] Figure 8 illustrates the schematic diagram of the assembly method of the solid-state supercapacitor. In addition, the electrochemical characterization results of the flexible solid-state supercapacitor cell are shown in Figure 9.

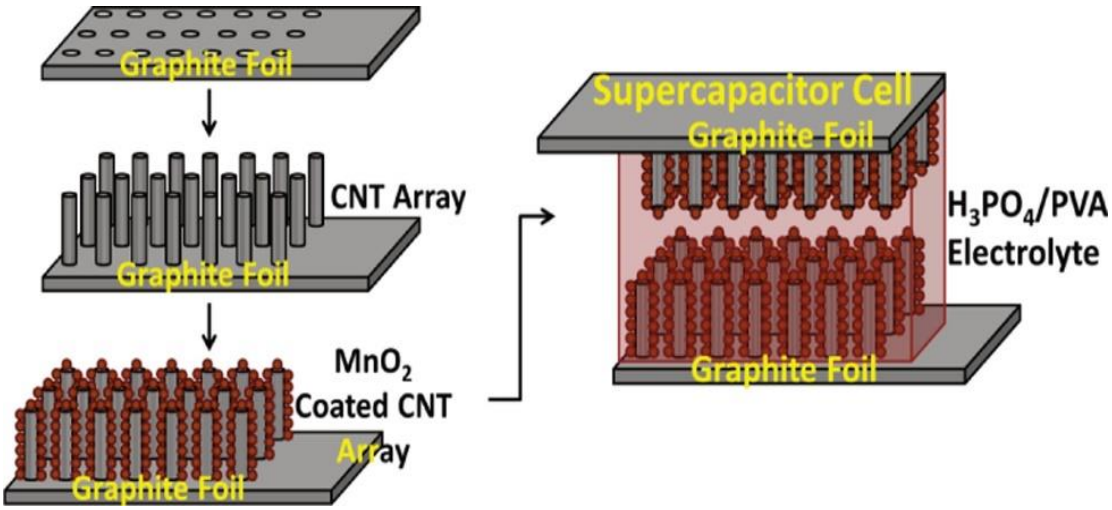

Figure 8. A schematic diagram presenting the fabrication method used to produce the solid-state supercapacitor in a sandwich and symmetric configuration.[78]

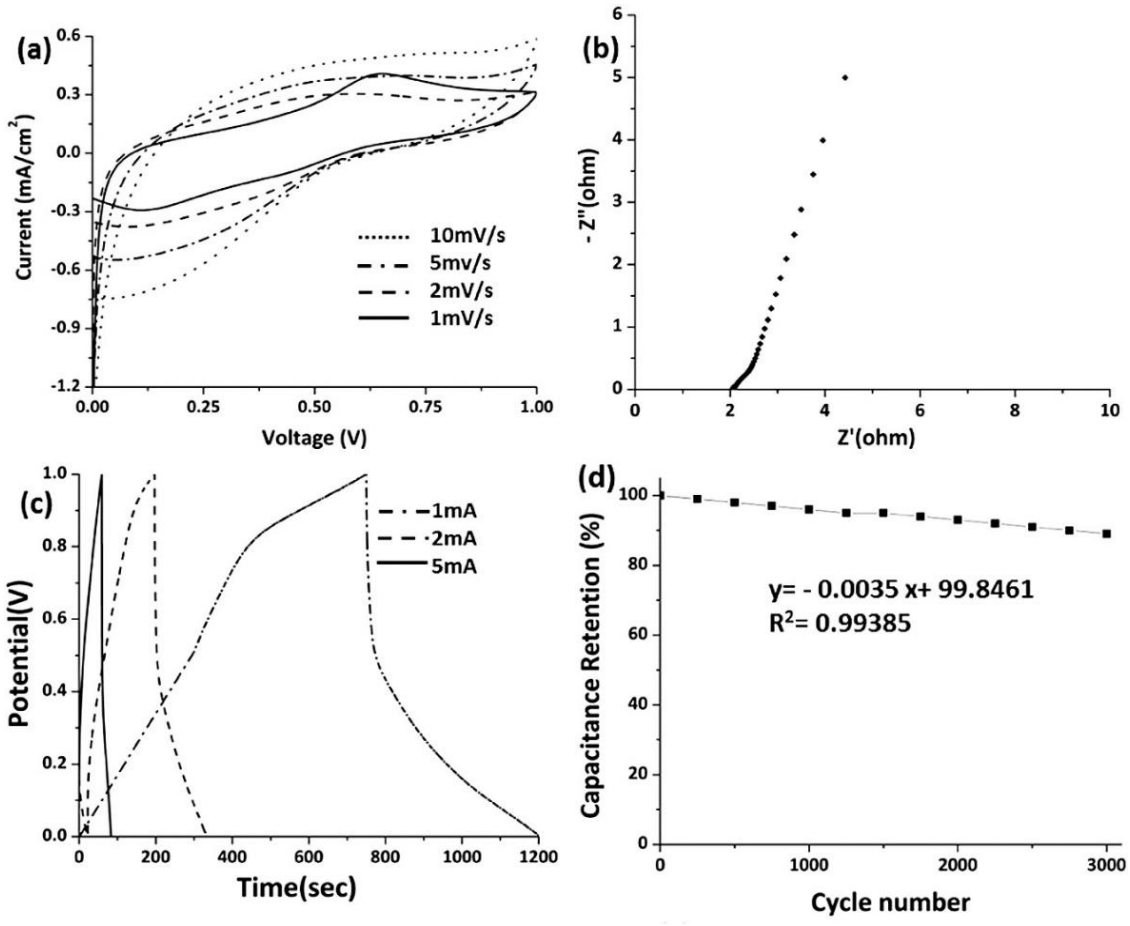

Figure 9. Electrochemical characterization shows (a) CV curves at different scan rates, (b) EIS, (c) charge/discharge at different current densities and (d) the cyclic stability of the flexible solid-state supercapacitor cell.[78]

Liu, W. et al. (2016) prepared ternary coaxial hierarchical nanofibers using the in-situ technique to synthesize the polyaniline (PANI) MWCNT. Then, MnO_2 deposited on PANI/MWCNT nanofibers to form ternary hierarchical nanofibers MnO_2/PANI/MWCNT.

The results presented that the specific capacitance of MnO_2/PANI/MWCNT composites reveals high capacitance of 348.5 Fg^{-1} at 1 Ag^{-1} and 88.2% of which can still be maintained after 2000 cycles.[79] Chen, J., and co-workers (2015) fabricated the 3D graphene/CNTs/MnO2 (GCM) nanocomposites electrode via a facile two-step method. The 3D forest-like rGO@CNTs (GC) functions as both ideal electron pathway and the backbone for MnO_2. The nanocomposites displayed a specific capacitance of 245 F g^{-1} at 0.5 Ag^{-1}, outstanding cycling stability with capacitance retention of 91.4% after 2000 cycles at a current density of 1 A g^{-1}. [80]

Xie X. and co-authors (2007)[81] fabricated MnO_2/MWCNT composite via in situ coating technique. Results demonstrated that a nanosized ε-MnO_2 uniform layer coated onto MWCNTs and the original structure of the pristine MWCNT was conserved through the coating process. The specific capacitance of the electrode exhibited around 250 F/g.

Hydrothermal method

Hydrothermal method states to any heterogeneous reaction in the existence of mineralizers or aqueous solvents under high pressure and high temperature (HPHT) conditions to dissolve and recrystallize the materials that are comparatively insoluble under ordinary conditions.[82,83] A ternary composite electrodes have been fabricated by Cheng, T., and co-authors (2017), which is nitrogen-doped graphene foam/carbon nanotube/manganese dioxide (NGF/CNT/MnO2), by chemical vapor deposition (CVD) with facile hydrothermal method. They proved the effect of MnO_2 mass loading in the production process and the nanoflake thickness in the electrochemical performance by loading 70% of MnO_2 which revealed a great areal capacitance and a high specific capacitance of 3.03 F/cm^2 and 284 F/g at the scan rate of 2 mV/s respectively. These results

showed that the reasonable proportion and the ultrathin flake-like structures of the MnO_2 are able to accomplish high specific areas, fast transport rate, and low aggregation resistance, which results in, high electrochemical performance. After the further tests, they found that the capacitance of the NGF/CNT/MnO_2 composite electrodes exhibited around 50% increase after 15,000 cycles.[84]

Recently, Shinde, P. et al. (2017) presented various nanostructured morphologies of MnO_2 coated onto carbon via hydrothermal method at altered deposition temperatures. The high specific capacitance of 595 F/g, with a specific surface area of 109 m^2/g, the areal capacitance of 4.16 F cm^{-2} at 5 mV/s was achieved at a temperature of 453 K Furthermore, over 2000 CV cycles, the MnO_2 weirds showed better cycling stability with capacity retention of 87 %. It has been demonstrated that the direct growth of highly porous MnO_2 weirds on carbon cloth enhanced the electrochemical performance.[85] Luo, X. and co-authors (2017) produced macroporous carbon material using mollusk shell material and deposit a thin layer of MnO_2 nanosheets via hydrothermal reaction to improve the performance of the electrode materials and supercapacitors. The electrode showed a high specific capacitance of 386 F/g at a current density of 1 A/g with an outstanding rate performance of 278.7 F/g at 10 A/g and a capacitance retention of 83% after 5000 cycles at 20 A/g.[86]

Sol-gel method

The sol-gel technique is used to produce highly controlled inorganic materials that are characterized by homogeneous morphology.[87–90] Remarkably, because of the great potential that can be achieved from sol-gel processes and the mild reaction parameters that can be used, both of hydrolytic and non-hydrolytic processes have been massively studied

for the synthesis of organic as well as inorganic materials.[91] Both of Reddy, R. and Reddy, R. (2004) reported the synthesis of amorphous MnO_2 via sol-gel method that occurred by reduction the $NaMnO_4$ with solid fumaric acid. The composition exhibited a maximum capacitance of 110 F/g at 5 mV/s in 2 M NaCl solution.[92]

Electrophoretic Deposition

Darari, A. et al. (2016) studied CNT-MnO_2 thin film designed by using electrophoretic deposition. They measured the capacitance of about 7.86 F. Figure 10 depicts the schematic of electrophoretic deposition method of CNT-MnO_2 deposited on the top of stainless steel foil.[93]

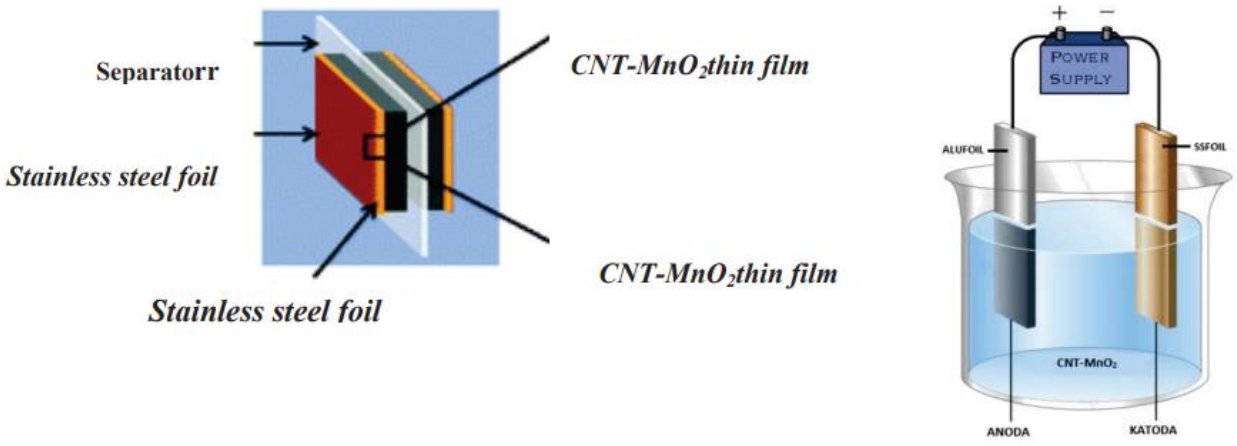

Figure 10. Electrophoretic Deposition Method Visualization.[93]

Dipping and drying

Successfully, Guo, G. et al. (2015) established a 3D porous CNT/MnO_2 composite electrode via a simple "dipping and drying" method.[94] After that, a potentiostat deposition technology used supercapacitor applications. By preparing a symmetrical supercapacitor using the novel electrodes, the composite electrode displayed a high specific capacitance of 160.5 F/g at 1 A/g and revealed an energy density of 22.3 Wh/kg at the power density of 500 W/kg, the electrochemical behavior of CNT/MnO_2 supercapacitor is shown in Figure 11.[95]

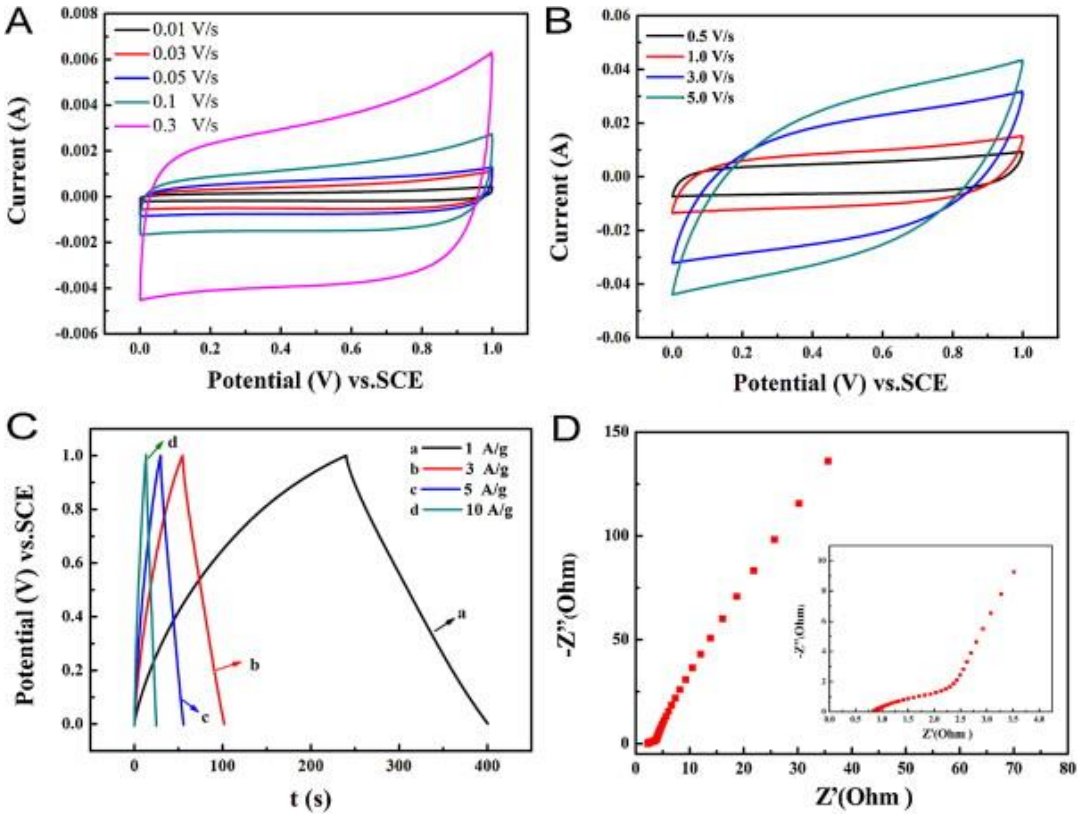

Figure 11. The electrochemical properties of CNTs/MnO_2 supercapacitor: A and B) CVs scanned at various scan rates, (C) GCD curves of CNT/MnO_2 supercapacitor at various current densities (D); the Nyquist plot of CNT/MnO_2 supercapacitor at open circuit potential. [95]

One-pot reaction process

Li, L., and co-workers (2014) produced MnO_2/CNTs composites by changed one-pot reaction method. In this method, the CNTs are coated homogeneously via cross-linked

MnO_2 flakes. The thickness of MnO_2 layers found about 50 nm with loading equal to 84% of MnO_2 on the CNTs surface. Additionally, the supercapacitive performance indicates that the composite exhibits an excellent specific capacitance of 201 $F.g^{-1}$ at 2 $A.g^{-1}$ in addition to excellent cycle stability at 1 $A.g^{-1}$ after 10 000 cycles since there was no capacitance decay. The as-assembled capacitor exhibited an elevated energy density of 13.3 $Wh.kg^{-1}$ at a power density of 600 $W.kg^{-1}$ in a voltage from 0 to 1.5 V.[96]

Simple vacuum filtration

Simple vacuum filtration deposition is widely used in supercapacitor applications.[97–100] Wu, P. et al. (2016) presented flexible films operated as pseudocapacitor electrodes by using a simple vacuum-filtration process to load δ-MnO_2 at CNTs layer. At 0.2 A/g which is the low discharge current density, the composite films revealed an excellent areal capacitance of 0.293 F/cm^2 and specific capacitance of 149 F/g with a mass of 1.97 mg/cm^2 and thickness of 16.5 μm. Furthermore, the films displayed a great rate capability with capacitance loss of 15% after increasing the discharge current from 0.2 up to 5 A/g^{-1}. After 5,000 cycles, the remaining cycling stability reached 90% of the initial capacitance.[101] Figure 12 presents the electrochemical behavior of MnO_2@CNTs/CNTs supercapacitor.

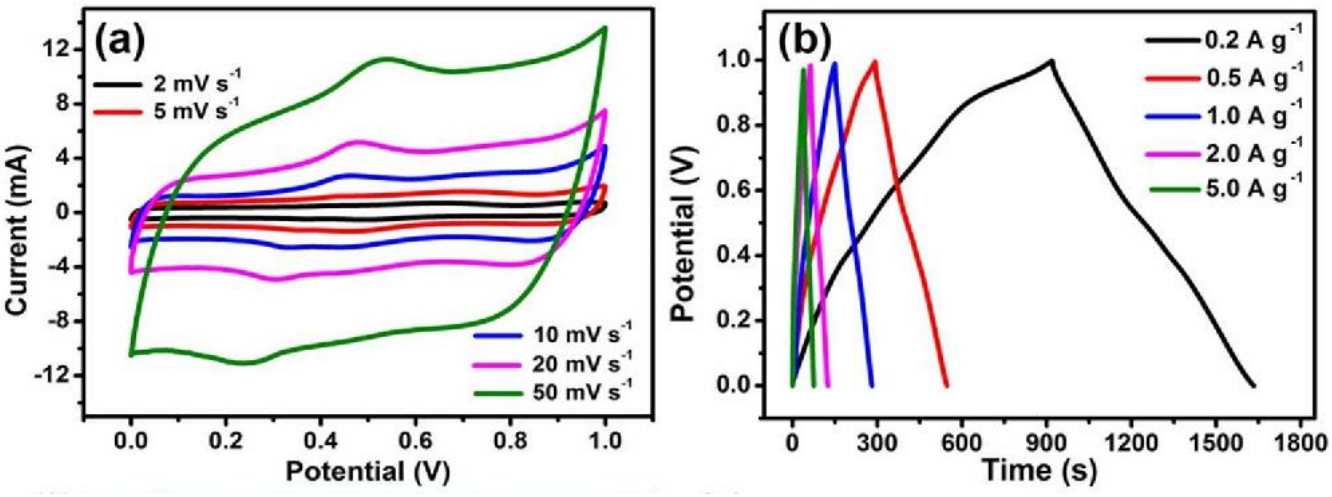

Figure 12. Electrochemical behavior curves of MnO_2@CNTs/CNTs film electrodes (a) CV at various scan rates; (b) GCD at different current densities.[101]

Particle extraction through a liquid-liquid interface (PELLI)

PELLI process supports the movement of the particles directly from an aqueous synthesis medium to an organic phase, therefore there no need for drying step and no agglomeration occurs for the particles.[102] In 2017, Chen, R. et al. fabricated CNT/MnO_2 composite by using PELLI method to synthesize non-agglomerated MnO_2 particles which gave advantages to produce a composite electrode through good dispersion of CNTs. The amount of mass loadings found in the range from 21 up to 50 mg.cm^{-2}. The analysis of capacitance data showed that the highest specific capacitance of 7.52 F.cm^{-2} was accomplished at 2 mV s^{-1} with the active mass loading of 47 mg cm^{-2}.[103]

Pulsed laser deposition

The preparation of less binder of electrode materials will help the energy storage devices to enhance the conductivity and/or facile process.[104,105] Ataherian, F. et al. presented a method to improve the capability of MnO_2 electrode using pulsed laser deposition under vacuum with varying the oxygen partial pressures. They found that the electrode made at a slow potential scan rate of 1 mV/s, with MnOx prepared under vacuum and 10 mTorr of O_2 provided specific capacitance as high as 738 and 653 F/g, respectively.[106]

In general, the chemical techniques used to deposit MnO_2 films on CNTs exhibit toxic solvents and reagents. In addition, the usage of binders and additive in these chemical processes leads to combining them with the active materials which reduce the supercapacitor capacitance. On the other hand, the Physical vapor deposition techniques such as sputtering are an environment-friendly and they produce contamination free metal oxide nanostructured materials. So, sputtering presents a successful method to synthesize high quality, binder free and eco-friendly nanostructures supercapacitor electrodes.

To the best of our knowledge, there is no report on using processes RF magnetron sputtering deposition technique to deposit a thin film of MnO_2 on CNTs sheet in order to produce flexible all solid supercapacitor.

CHAPTER 3: EXPERIMENTAL WORK

3.1 Materials

- Carbon nanotubes (CNTs) material
- Ethanol
- Ferrocene
- Sulfur
- Manganese dioxide, MnO_2 (99.9%, size F59.8 × 4 mm) target used for RF sputtering was purchased from Plasma Technology Limited (PTL).
- Sodium sulfate Na_2SO_4 (142.04 g/mol) were purchased from BDH laboratory supplies.
- Sulfuric acid, H_2SO_4 (98%) were purchased from BDH laboratory supplies.
- Ortho-phosphoric acid H_3PO_4 (85%) from Fluka.
- Polyvinyl alcohol (PVA) (MW 60000 Da) was obtained from Merck.

3.2 Experimental Work

3.2.1 Material Preparation

Working electrode synthesis

Carbon nanotubes are manufactured via floating catalyst chemical vapor deposition (CVD) method. The ethanol is used as the main carbon source. Iron catalyst particles used after dissolving the ferrocene in the fuel, which avails as the source for the catalyst. Sulfur is used as the catalyst conditioner. The fuel mixture is inoculated into the furnace in the existence of hydrogen. After that, the vaporized fuel mixture is collected through controlled thermal gradients to create a tight distribution of the appropriate size catalyst particles and

to remove the ethanol to produce a carbon source to utilize it in the nanotubes. The growth of nanotubes is endured through the furnace and then combined onto a moving drum until the desired dimensions are achieved. Lastly, CNTs sheet is removed from the furnace and used in the work.[107] CNTs were cut into the small sheet. To remove impurities, CNTs sheet was thermally annealed at 400 ^{o}C for 6 hours under Ar gas (MTI corporation, GSL 1500X-OTF). MnO_2 thin film was deposited on CNTs fabric using RF magnetron sputtering technique (JCP-350M2).

The sputtering chamber was at first evacuated to a base pressure of 8×10^{-3} Pa. Thereafter, the sputter deposition was achieved at a pressure of 0.4 Pa under a constant flow of Ar of 6 sccm. The deposition was carried out for one hour, two hours and three hours applying constant RF power of 150W at room temperature. During the sputtering process, the substrate was rotated to confirm a uniform distribution of MnO_2. The mass of MnO_2 deposited on CNTs fabric was determined by mass difference before and after sputtering using microbalance (Mettler Toledo™ Excellence Plus, XPE Series).

3.2.2 Fabrication of symmetric all-solid CNTs/MnO_2 supercapacitor

The symmetric all solid supercapacitor was prepared by assembling two identical CNTs/MnO_2 fabrics separated with PVA-H_3PO_4 gel. The PVA-H_3PO_4 gel was prepared by mixing 8 g of H_3PO_4 and 10 g PVA powder in 100 mL of deionized water. The mixture was heated to 90^{o}C under vigorous stirring until a transparent gel was obtained as shown in Figure 13. The MnO_2 face of each CNTs/MnO_2 electrode was coated with PVA-H_3PO_4 gel, dried at room temperature overnight, and then MnO_2 face-to-MnO_2 face assembled.

The electrical connection was assured by connecting CNTs face of each CNTs/MnO_2 electrode with copper foils as shown in Figure 14.

Figure 13. PVA-H_3PO_4 gel preparation

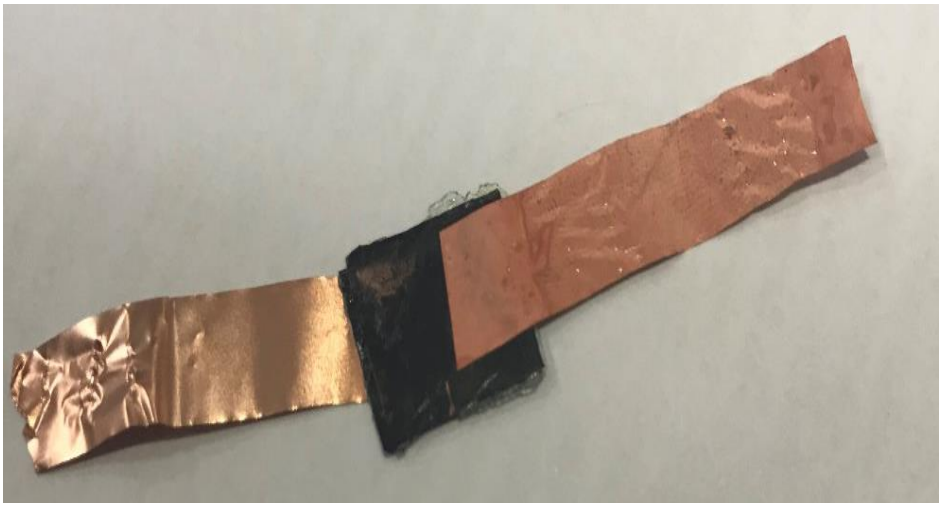

Figure 14. Assembled CNTs/MnO_2 electrodes with copper foils

3.2.3 Characterizations

3.2.3.1 RF sputtering technique

Sputtering technique is a physical vapor deposition technique. [108] It is used to produce thin films of metals, alloys, nitrides, carbides or oxides materials.[109] The sputtering process starts by creating a gaseous plasma. This is achieved by application of power (DC or RF). These gas ions have high energy and are attracted to the target. The bombardment of the gas ions with the target leads to the ejection of target atoms. In magnetron sputtering, very strong magnets are used to produce magnetic fields that confine the electrons in the plasma at or near the surface of the target. The ejected atoms will have enough kinetic energy to reach the surface of the substrate creating the desired thin film as shown in Figure 15.

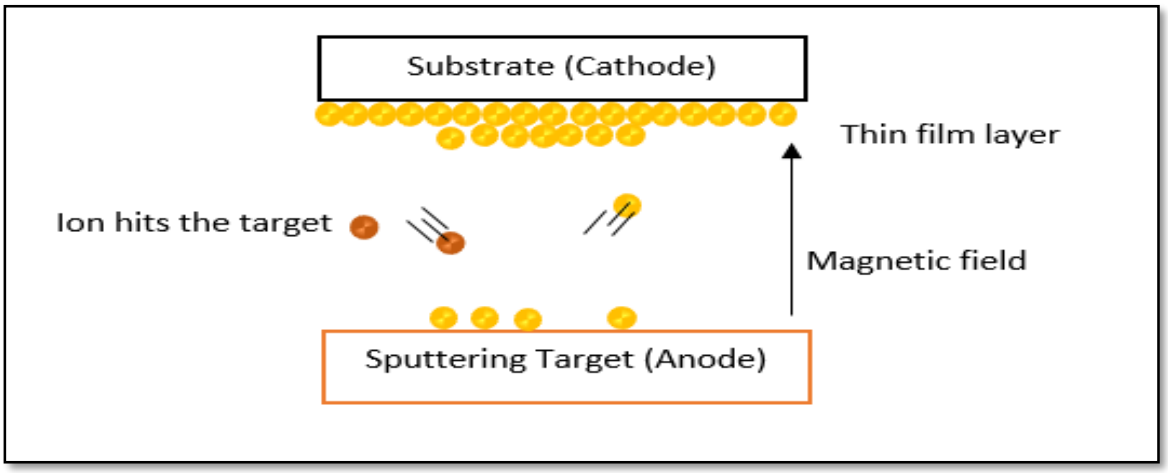

Figure 15. Illustrative drawing of a magnetron sputtering technique.

The magnetron sputtering technique offers great advantages compared with other techniques such as uniform, homogeneous and great adhesion deposition over the comparatively large area, ability to choose the substrate material and target material with very high melting points and high deposition rate. [110] Figure 16 illustrates the main factors used to tune the thickness of the synthesized films in sputtering technique. These factors are the integrated pulse energy, deposition time, [111] chamber pressure, plasma gas, angle of target and the substrate, and substrate temperature which is important to reduce the dopant redistribution and defect formation related to high-temperature processing.[112] Figure 17 shows the RF magnetron sputtering machine used in this work.

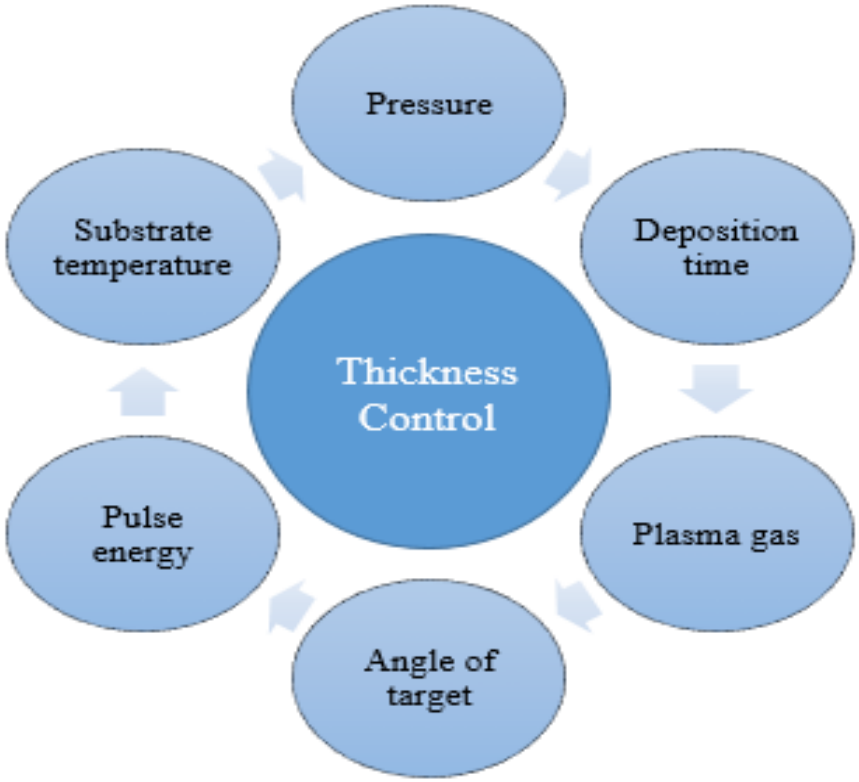

Figure 16. Main factors to tune the thickness of the synthesized films in sputtering technique

Figure 17. RF magnetron sputtering machine

3.2.3.2 Scanning Electron Microscope (SEM)

Sample's morphology is characterized by using scanning electron microscope (SEM). It works by scanning the surface of the sample with a focused beam of electrons to create an image. Then the electron beam interacts with sample generating different signals as shown in Figure 18. Secondary electrons detector is used for detecting the secondary electrons released from the sample. These electrons are attracted to a high voltage of about

10kV are amplified, modified into a signal and then transferred to the display unit producing SEM image of the sample.[113] Different output signals can be measured for instance secondary electrons, forward-scattered and back-scattered electrons, and X-rays. The results were conducted by Scanning electron microscopy (SEM) and energy-dispersive X-ray spectrometry (SEM, Nova Nano SEM 450) with a voltage of 500 V to 30 KV. The distance between the electron beam and the sample was 10 mm to obtain good images.

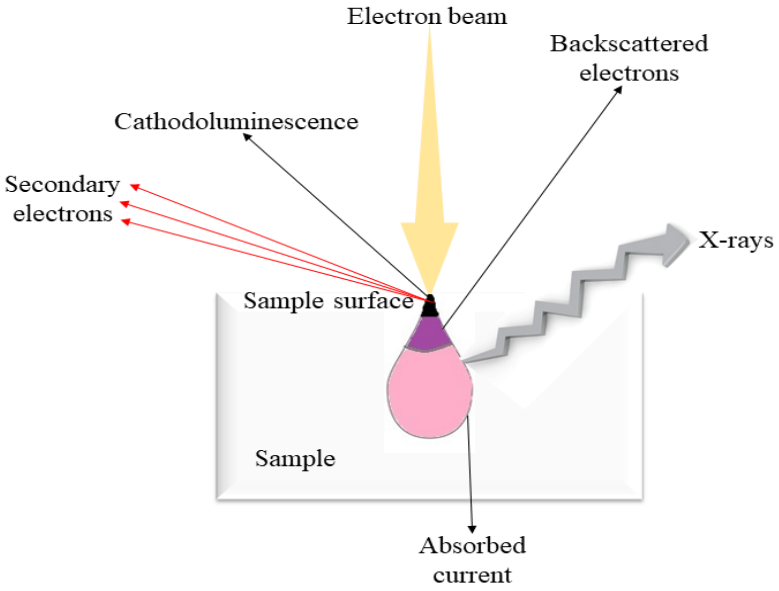

Figure 18. Mechanism of scanning electron microscopy

3.2.3.3 Energy Dispersive Spectroscopy (EDS)

Energy Dispersive Spectroscopy (EDS) or (EDX) technique is an analytical technique used to analyze the elements of samples. EDS depends on bombarding the sample with a focused beam of electrons that producing X-ray spectrum to generate a chemical analysis and identify the elemental compositions. Moreover, there are two analysis types in EDS; qualitative analysis contains the identification of the X-ray lines in the spectrum and quantitative analysis that determines the concentrations of each element by measuring line intensities.

3.2.3.4 Raman Spectroscopy

Materials are interacting with the light causing an incident light absorbed, scattered, reflected, or pass through the material. Raman spectroscopy is a technique applied to measure the wavelength and intensities of inelastically scattered light by measuring the change in rotational, electronic energy or vibrational of a molecule. The Raman scattering works when a photon is an incident on a molecule then it combines with the electric dipole of that molecule and undergoes a frequency shift (gain or loss of energy). This frequency shift of the scattered photons results from exciting the vibrational state of molecules in the material. In Raman spectroscopy, two types of scattering lines present; Stokes lines exist when the lines of frequency shorter than the exciting lines and the others anti-Stokes lines as shown in Figure 19.[114,115] The results of Raman spectra are performed via Thermo Fisher Scientific (DXR™2 Smart) at a laser wavelength of 532 nm.

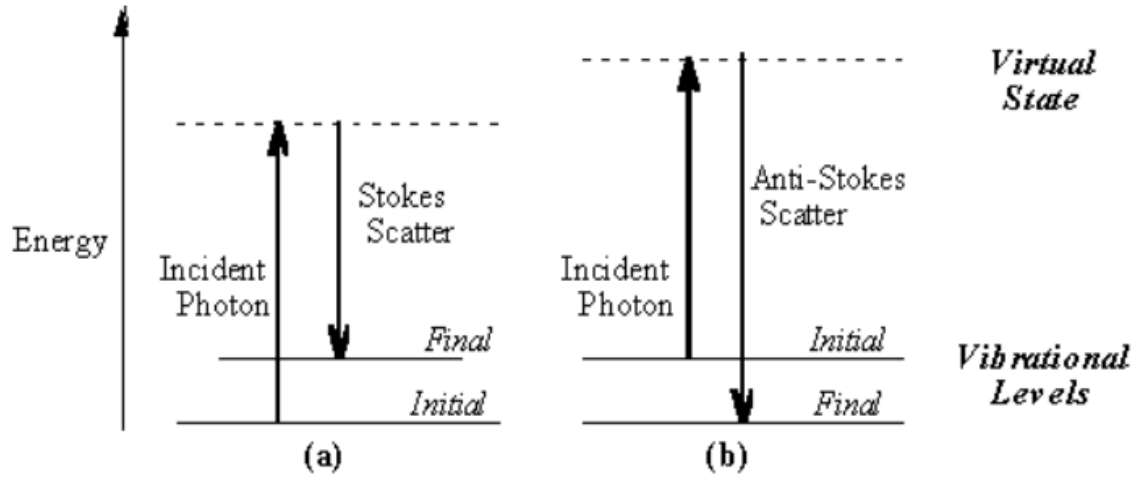

Figure 19. Raman scattering diagram presenting the energy level for; (a) Stokes scattering, (b) anti-Stokes scattering

3.2.3.5 X-ray diffraction (XRD)

X-ray diffraction (XRD) is a nondestructive technique used to analyze a crystal structure of materials and depends on the diffraction of an incident X-ray beam. Bragg's law relates the x-rays wavelength, the lattice spacing of the crystal and the diffraction angle; so at Bragg conditions when x-rays scattered through the crystalline material, they interfere out of certain crystalline planes in a certain direction which is the diffraction angle (angle between the incident x-rays and the. The following relation is describing the Bragg's law:

$$n\lambda = 2d \sin \theta \quad (3)$$

where n is an integer number (the order of diffraction), λ is the wavelength of the incident wave, d is the spacing between consecutive parallel planes, and θ is the incident angle. Hence from Bragg's equation, the lattice spacing can be calculated. Figure 20 presents the schematic-representation-of-the-Bragg-equation.

XRD measurements were accomplished via PANalytical diffractometer and Bragg-Brentano configuration. The X-ray source is generated in the tube using Copper anode which is the most common target material due to its coverage range and its Cu-Kα radiation wavelength is 1.5405Å. The scans were operated using high voltage of 45 kV for the tube, current equal to 20 mA at a scan rate of 2°/min with a diffraction angle 2θ between 10° and 80°.

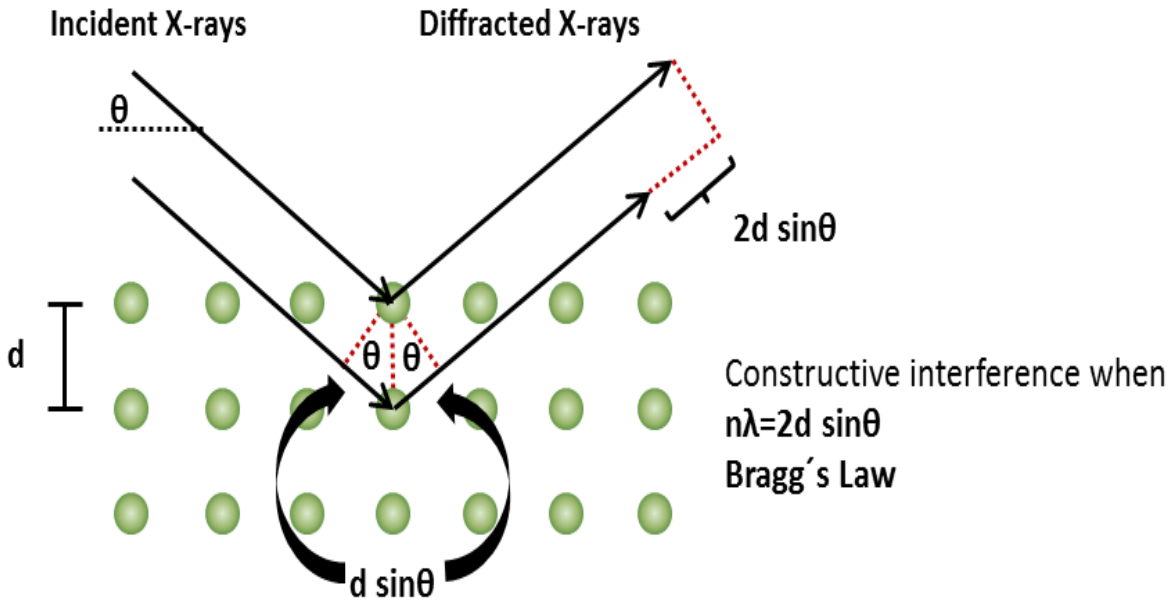

Figure 20. Schematic illustration of the-Bragg-equation

3.2.3.6 X-ray photoelectron spectroscopy (XPS)

X-ray photoelectron spectroscopy (XPS) is an important method for the semi-quantitative analysis of surface composition that can investigate a sample to a depth of 2 to 5 nanometers (nm). Because of its features in estimating the chemical state and compositions, therefore, XPS used to study metallurgy, microelectronics, heterogeneous catalysis, corrosion science and polymer technology.[116] In addition, XPS detects the surface's chemical elements in addition to the chemical bond natures that occurs between these elements. It can reveal all the elements except helium and hydrogen. Figure 21

demonstrates the main components of an XPS mechanism which are a light source, an electron detector and an electron energy analyzer. XPS measurements were conducted via X-ray photoelectron spectroscopy (XPS; AXIS Ultra DLD (XPS). The X-ray source is equipped with a monochromated Al-kα and a spherical mirror analyzer with the ability to map the surface with a spatial resolution below 3 μm.

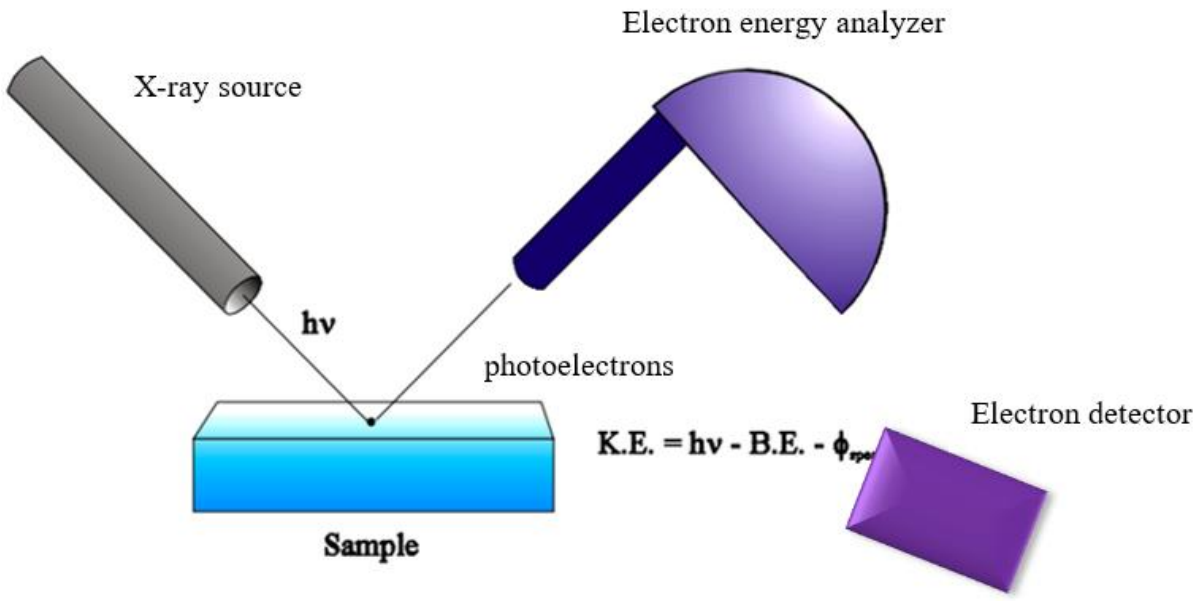

Figure 21. Basic elements of XPS experiment

3.2.3.7 Mechanical test

Mechanical properties are a great concern in detection the materials behavior, especially in engineering applications. It's used to study the characteristics of the material such as hardness, strength, and toughness.[117] The tensile test is considered as a basic and a worldwide engineering test, where it used to investigate the material parameters. Some important parameters such as Young's modulus, yield strength, ductility, toughness and strain rate can be achieved using the test. These parameters are useful for engineers to select the suitable materials for specific application.[118] The particular material usually displayed the relationship between the stress and strain which presented in the stress-strain curve. Each material has a unique curve represent its properties and is found by measuring the amount of deformation known as strain at distinguished intervals of tensile stress or compressive loading stress. Figure 20 reveal stress-strain curve demonstrating the properties of a material. The tensile test performed for several reasons such as in material specifications to maintain the quality.

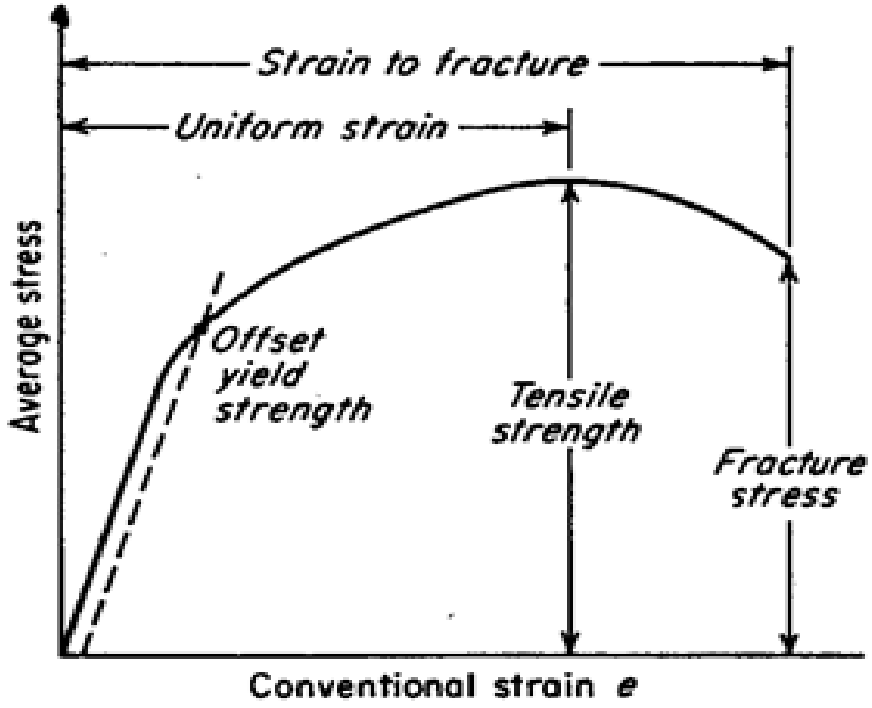

Figure 22. Stress–strain curve

3.2.3.8 Cyclic voltammetry (CV)

An electrochemical characterization technique used widely in research field because of its effectiveness and ability to measure the current over a wide potential range. CV technique records the potential of the working electrode (varied among minimum and a predetermined maximum potential) as it is cycled over time and measuring the resulting current. Repetitively, the electrode potential of CV test sweeps between two peak values specify the number of cycles. A pair of sweeps in opposite directions (forward and reverse

scan) is called a cycle. Moreover, the change of potential with time named with scan rate (v), measured from the slope with unit mV/s. As the scan rate increases, the voltammogram curve turns into tilted and the ohmic resistance is highly prominent, which lead to affect the forming of the double layer in the capacitors and store the charge in the electrode.[119] Besides that, the potential of the working electrode is measured against a reference electrode (have a constant potential). Also, the potential range is affected by the type of the electrolyte, for example, in an aqueous solution, the maximum potential will be held around 1V to avoid the electrolysis of water (1.23V). While the non-aqueous solution potential range can be extended to approximately 3V in theory.[119]

3.2.3.9 Electrochemical Impedance Spectroscopy (EIS)

The measurement of the capability of a circuit to resist the flow of electrical current is called impedance. To study the resistance, Ohm's law state it in terms of the ratio between potential, E [V], and current, I [A]:

$$R = \frac{E}{I} \qquad (4)$$

which valid only for ideal resistors, and independent of phase, frequency, and follows the relationship of the previous equation for any current and voltage. However, Ohm's law cannot explain the performance of more complex circuits. So, electrochemical impedance spectroscopy (EIS) describes the system response after applying a small periodic AC signal to the electrochemical cell with several frequencies are ranged from tens of mHz to MHz. Then it measures the emerging current passing through the cell. Studying EIS system offers important information about the EDLC interface and its chemical reactions. Furthermore,

since the excitation signal is very small, a linear or pseudo-linear response can be predictable. While the current response to a sinusoidal potential will be a sinusoid with an equal frequency but phase-shifted as illustrated in Figure 23.[119]

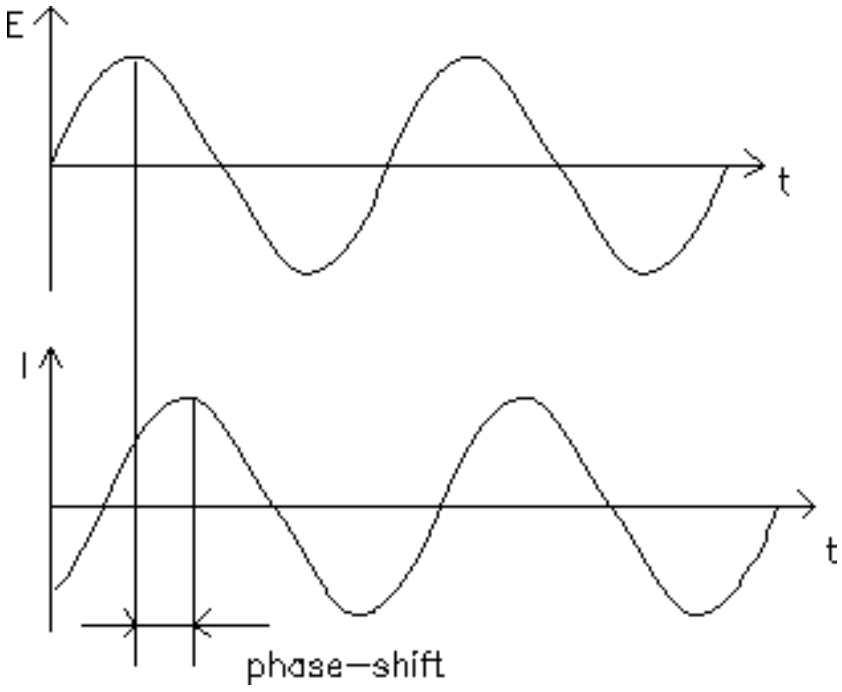

Figure 23. Sinusoidal Current Response in a Linear System

3.2.3.10 Galvanic charge/discharge (GCD)

GCD technique records the potential of the working electrode as it is cycled over time. The curve then gives an exemplary excitation signal and the triangular shape. The following formula is used to determine the specific capacitance from the charge-discharge curves in two electrodes symmetric cell configuration:[120]

$$SC=2(\frac{I.\Delta t}{m.\Delta V}) \quad (5)$$

where I represent the charge or discharge current, Δt is the charge or discharging time, m is the active mass of one electrode, and ΔV is the voltage drop upon discharging. Moreover, to determine the specific capacitance from the charge-discharge curves in three electrode configuration from the equation: [120]

$$SC = \frac{I.\Delta t}{m.\Delta V} \quad (6)$$

where I exemplify the charge or discharging current, t is the charge or discharge time, ΔV is the potential drop during discharge, and m is the mass of active material in the working electrode. This is the most common test on a cell to determine its capacity besides, the life cycle of a cell. Also, the test examines the performance of the cell after the charge transfer over a number of charge/discharge cycles. The supercapacitor will also exhibit self-discharge over time that can be measured for a long time period.[121]

3.2.4 Performance Testing

Figure 24 shows the CorrTest electrochemical workstation instrument (CorrTest instruments, Chine) which was used to perform all electrochemical measurements. The measurements were achieved at room temperature 20±1 ºC using a glass beaker with 1M

H_2SO_4 acidic solution for studying raw CNTs and 1M Na_2SO_4 aqueous solution as an electrolyte for studying CNTs/MnO_2 composites and three-electrode configuration. A circular shape of CNTs and CNTs/MnO_2 electrode with a surface area of 0.5 cm^2 applied as working electrodes, a saturated calomel electrode (SCE) served as the reference electrode and graphite bar availed as the counter electrode. CV measurements were taken at various scan rates (5, 10, 50, 100, and 200) mV/s within the potential range of 0 to 1 V for five cycles. EIS was achieved in the 10^5 to 0.0001 Hz range with voltage Amplitude 100 mV and 20 steps/decade. At last, GCD applied at various scan rates (0.5, 1, 2, 5, and 10) mA/mg by maintaining a potential range between 0 to 1 V vs reference electrode. The specific and facial capacitance of MnO_2 is calculated from both CV and GCD.

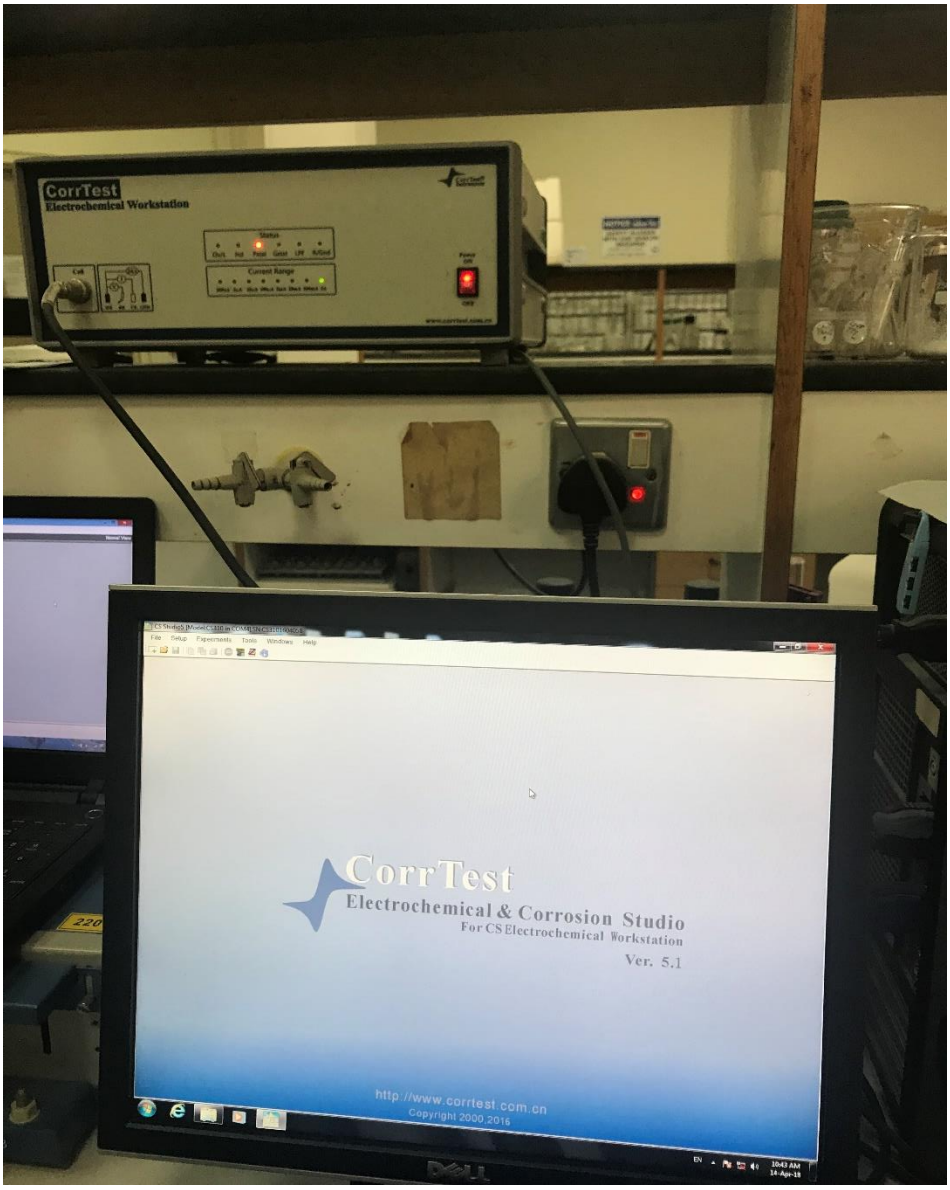

Figure 24. CorrTest electrochemical workstation instrument

CHAPTER 4: RESULTS AND DISCUSSIONS

In this work, three different thicknesses of MnO_2 350 nm, 700 nm, and 1000 nm have been prepared on CNTs surface using RF magnetron sputtering technique to produce flexible CNT/MnO_2 hybrid film. The obtained sheet is utilized as a working electrode to improve the performance of supercapacitors. The electrode synthesis is done in two steps, CNTs sheet produced via floating catalyst chemical vapor deposition (CVD). Followed by deposition of MnO_2 on CNTs sheet by RF magnetron sputtering. The effect of MnO_2 thickness on the electrochemical and mechanical properties of CNTs/MnO_2 hybrid material is evaluated. In this chapter; results and discussion are divided into the following sections:

- Preparation of CNTs/MnO_2 composites.
- Characterization of CNTs/MnO_2 composites using Raman, XRD, SEM and Tensile test.
- Electrochemical performance of CNTs/MnO_2 composites using CV, EIS, and GCD.

4.1 Materials Characterization

CNTs sheet and CNTs/MnO_2 composite were examined using Raman spectra, XRD spectra, and SEM. As displayed in Figure 25a, the CNTs revealed three distinctive Raman bands, D, G and G' bands, at 1366, 1583 and 2724 cm^{-1} respectively.[122] D band represents defects originating from disordered carbon. G and G' bands represent graphitic planes.

The D-band to G-band intensity ratio is 0.42 presenting the crystallinity of the pristine CNTs,[123] the intensity ratio of the D to the G band (I_D/I_G) offers a sensitive measure of the crystallite size and the qualitative change of defect content in CNTs layers.[124] Raman spectrum of CNTs/MnO_2 with different thicknesses were studied. Figures 25b-d show that the all CNTs/MnO_2 with different thicknesses exhibit a band at 645 cm^{-1} related to birnessite-type manganese dioxides (δ-MnO_2), in agreement with one major vibrational features of the birnessite-type MnO_2 compounds previously reported at 625 to 650 cm^{-1}.[125,101]

Furthermore, the spectra of both samples with 350 nm and 700 nm thick MnO_2 exhibit D, G, G' band peaks with identical D to G ratios of 0.98. The sample with 1000 nm thick MnO_2 does not exhibit any peak related to CNTs because of the thick MnO_2 layer.

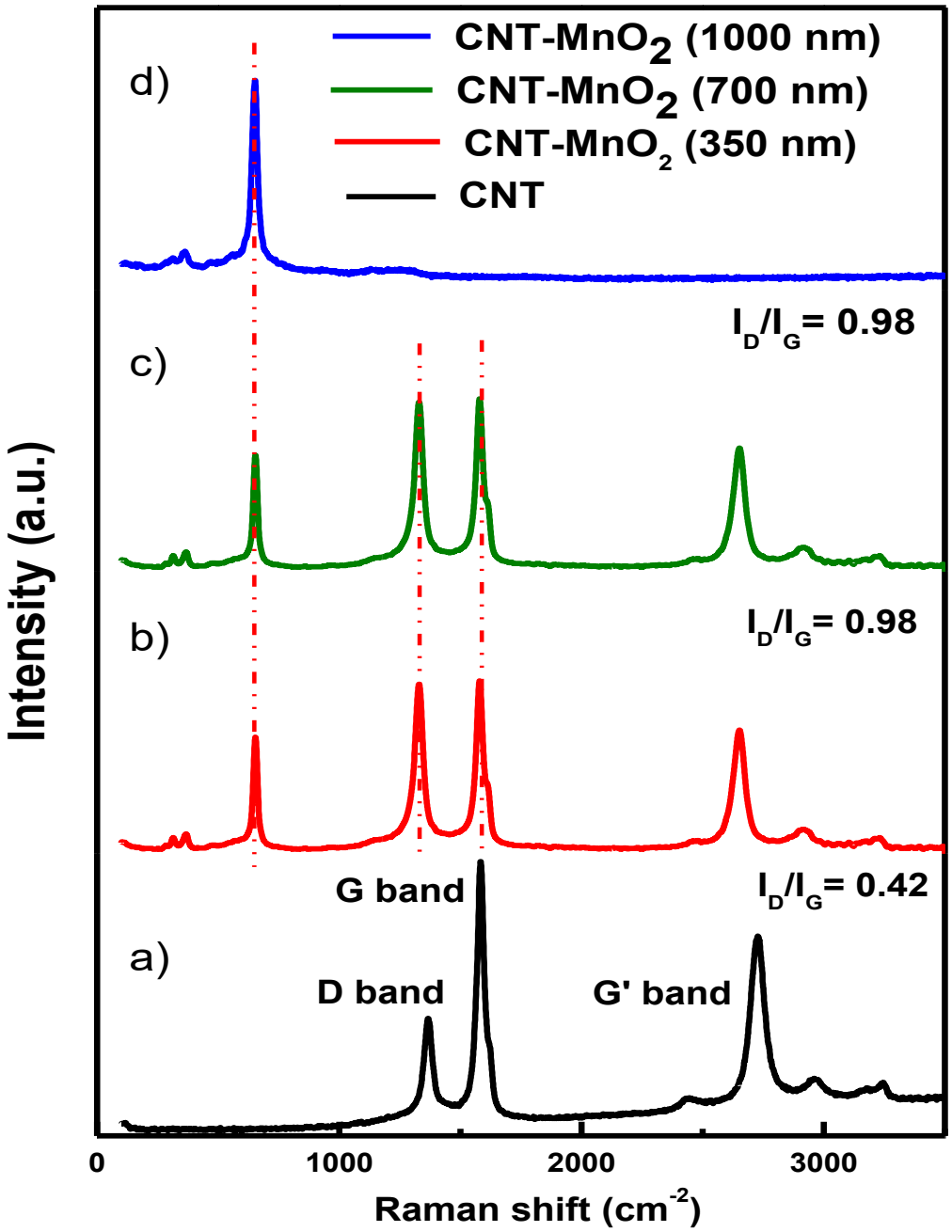

Figure 25. Raman spectra of a) CNTs and CNTs/MnO_2 with different MnO_2 thickness b) 350 nm, c) 700 nm and d) 1000 nm.

The XRD patterns of CNTs sheet and CNTs/MnO_2 composite are presented in Figure 26. It can be noticed that CNTs exhibited a sharp peak at 26^o which corresponds to (002) planes with an interplanar spacing of 3.36 A$^\circ$ and another weak peak at 44.47^o corresponds to (100) planes with an interplanar spacing of 2.04 A$^\circ$.[126] These peaks are characteristic of the graphite structure and can be distinguished from the others of the CNTs/MnO_2 on the XRD pattern.[34,127] The peaks of CNTs/MnO_2 composites at 18^o, 35.8^o and 38^o correspond to the crystal planes of (001)[128], (20$\bar{1}$), and (003) planes in MnO_2 layered birnessite respectively.[101] The (002) peak of CNTs is clearly seen in the XRD pattern of CNTs/MnO_2 indicating that the deposition of MnO_2 to CNTs did not affect their phase structure.[101]

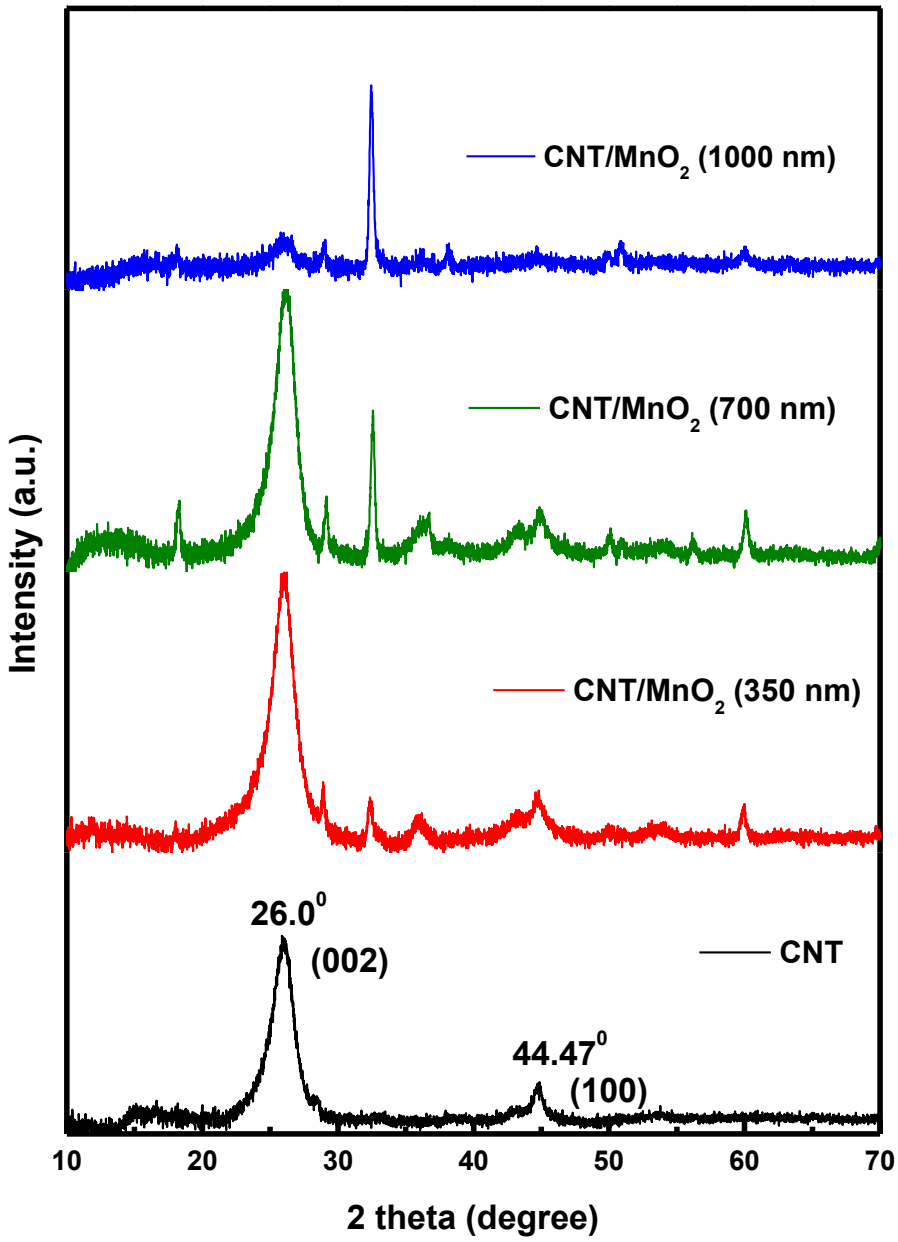

Figure 26. XRD patterns of CNTs (black) and CNTs/MnO_2 of different MnO_2 thickness (red;350 nm, green; 700 nm, blue; 1000 nm).

In order to reveal the chemical state analysis and further detail of the elemental composition of the sputtered film, XPS measurements were conducted.

The acquired XPS full spectrum (Figure 27a), displays signals from Mn, O, N and C elements, indicating the existence of MnO_2 on the surface of CNTs. The high-resolution XPS spectrum of Mn 2p (Figure 27b) exhibits two peaks at 640.1 eV and 651.9 eV (11.8 eV energy separation) corresponding to Mn $2p_{3/2}$ and Mn $2p_{1/2}$, respectively.[46,129] This confirms an oxidation state of +4 (Mn^{4+}) for Mn in the sputtered film, which is in agreement with MnO_2 formula. While the spectrum in Figure 27c shows the high-resolution Mn 3s core level. The energy separation is equal to 5 eV corresponding to MnO_2[13,14,15].[130]

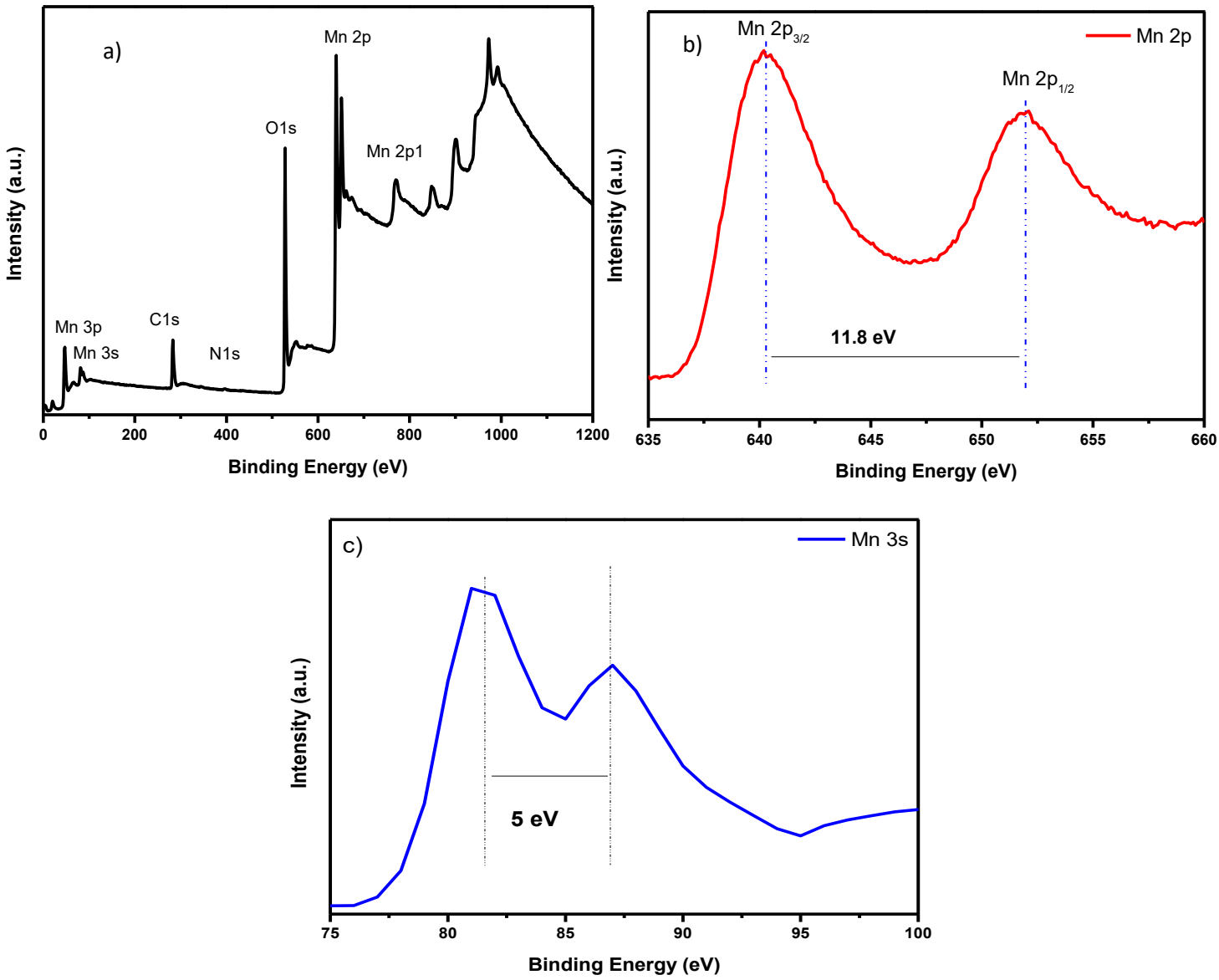

Figure 27. XPS of 1000 nm MnO_2 thickness of the CNTs/MnO_2 sample (a) full spectrum, (b) Mn 2p and (c) Mn 3s.

The morphology of the fabric obtained after MnO_2 sputtering was examined by Scanning electron microscopy (SEM) and energy-dispersive X-ray spectrometry (EDX).

Figure 28 shows SEM images of CNTs at the scale of 3 µm (Figure 28a) and CNT/MnO_2 fabric with different MnO_2 thicknesses at the scale of 4 µm (Figure 28b-d.) Figure 28b shows that the surfaces of CNTs nanowires are totally covered by MnO_2 producing a shape of worms after one-hour deposition which results in 350 nm thick MnO_2 with clear interparticle boundaries. As the sputtered time increased to 2-hours (700 nm), almost the whole surfaces of CNTs nanowires are covered (Figure 28c.). Further increase in sputter time (3 hours) results in a uniformly distributed MnO_2 on the surface of CNTs nanowires with a complete coverage of the CNTs network (Figure 28d). The cross-sectional SEM image (Figure 28e) of the sample with 3-hour deposition time, reveals a 1000 nm thick MnO_2 film homogenously deposited on the surface of CNTs fabric.

In order to confirm the elemental composition of the film, the SEM and corresponding EDS mapping images are shown in (Figure 29 a-d) which presents the presence of C, Mn and O_2 are well distributed in the structure fabrics.

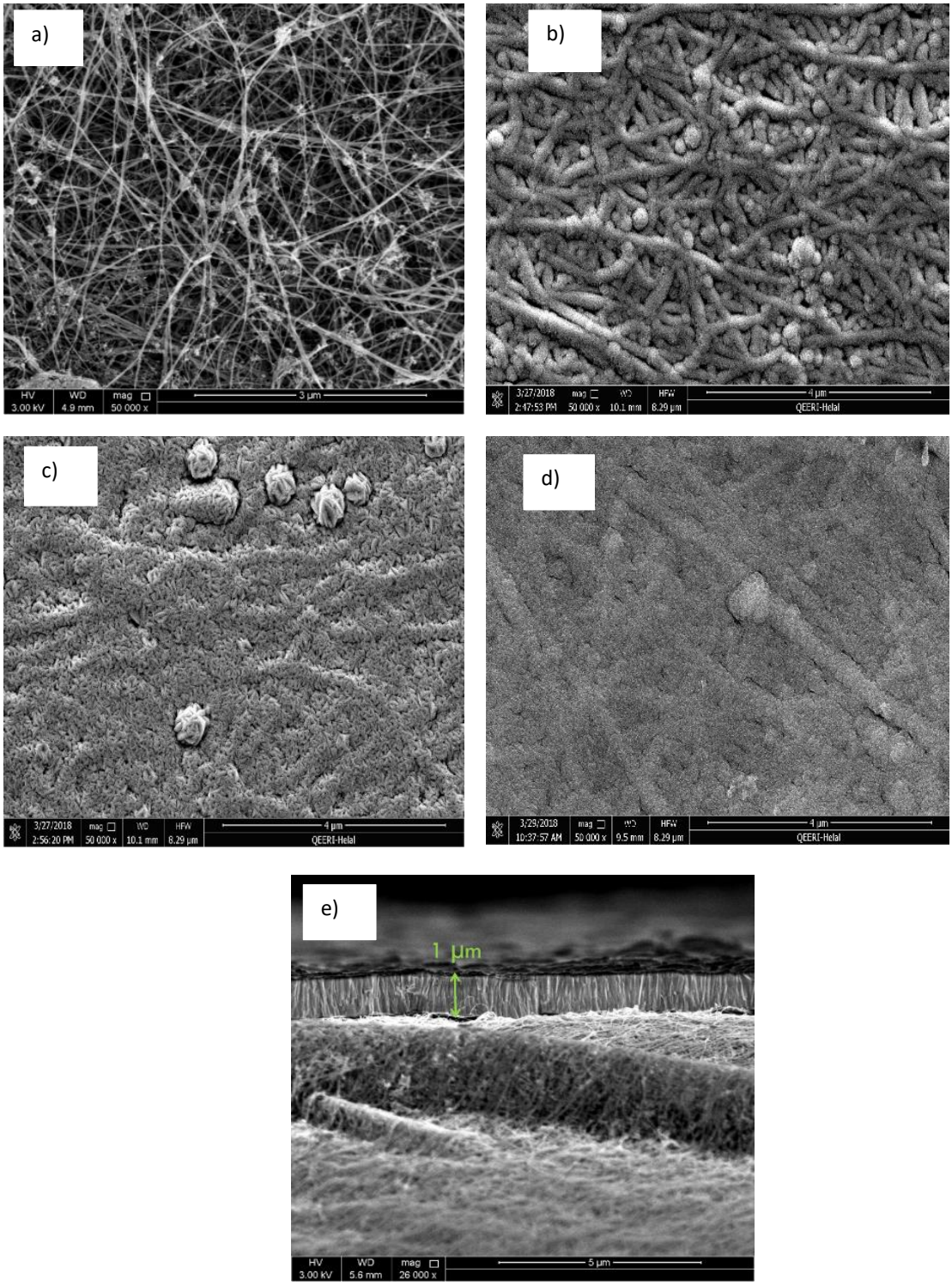

Figure 28. SEM images of (a) raw CNTs, (b) CNTs/MnO_2 composite with 350nm thick of MnO_2 (c) with 700nm thick of MnO_2 (d) with 1µm thick of MnO_2.

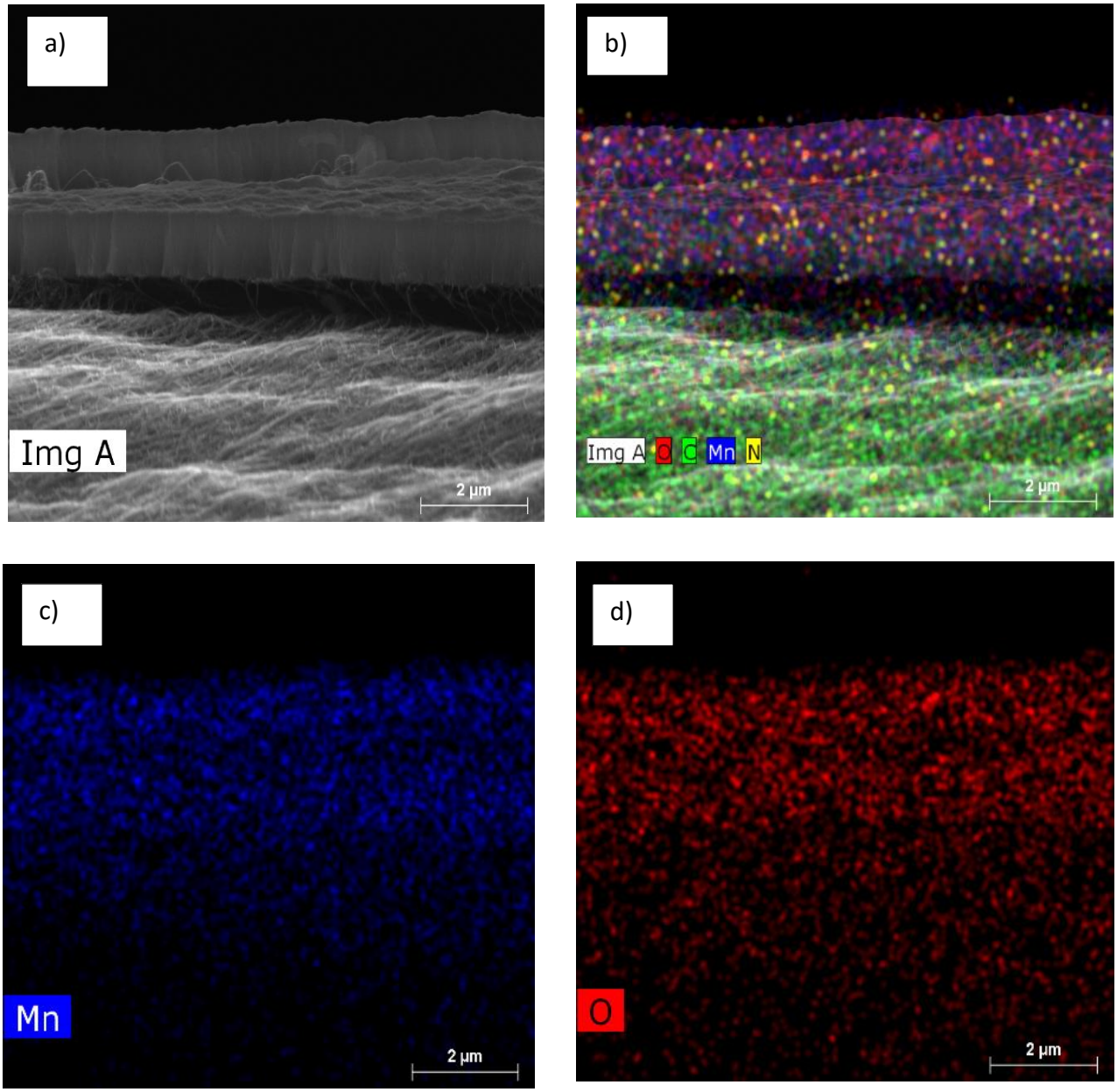

Figure 29. SEM images for (a) cross section of CNTs/MnO_2, SEM mapping of (b) CNTs/ MnO_2, (c) Mn and (d) O_2.

The suitability and compatibility of the as-prepared CNTs/MnO_2 composite material (with 1000 nm thickness) was evaluated by tensile test to be applied as an electrode material in flexible and wearable supercapacitors. From the load applied versus elongation, the stress-strain curve can be obtained and the flexibility can be meauresed[1316]. Moreover, various mechanical properties such as elastic modulus, ultimate tensile stress and ductility may be calculated. Figure 30a presents stress-strain curves of CNTs and CNTs/MnO_2 composite with 1000 nm thick Mno2. The elastic region could be measured from the linear part of the curve, in this region, the atomic bonds of the material are stretched. Young's modulus (the slope of the elastic region) increased from 10 MPa for the CNTs fabric and to 15 MPa for CNTs/MnO_2 composite material. This result indicates that the elasticity of the CNTs fabric is enhanced after the deposition of 1000 nm MnO_2 thin film by RF magnetron sputtering. The ultimate tensile strength is 23.8 MPa for CNTs fabric, and 34.7 MPa for CNTs/MnO_2 composite material. Furthermore, the plastic region is wider in CNTs/MnO_2 composite material (23% strain) compared to that of CNTs fabric (16% strain), which indicates that the failure strain is greater for CNTs/MnO_2 composite material. Additionally, due to high conductivity and high porosity of CNTs, the flexibility of one-unit film bent to numerous angles of 0°, 45°, 90°, and bent at 180° which also did not effect after sputtering MnO_2. (seen in Figure 30b, the corresponding schematic optical images of CNTs/MnO_2 films). These results are favorable for the improvement of flexible and wearable devices profiting from the excellent mechanical properties of CNTs/MnO_2 composite material.

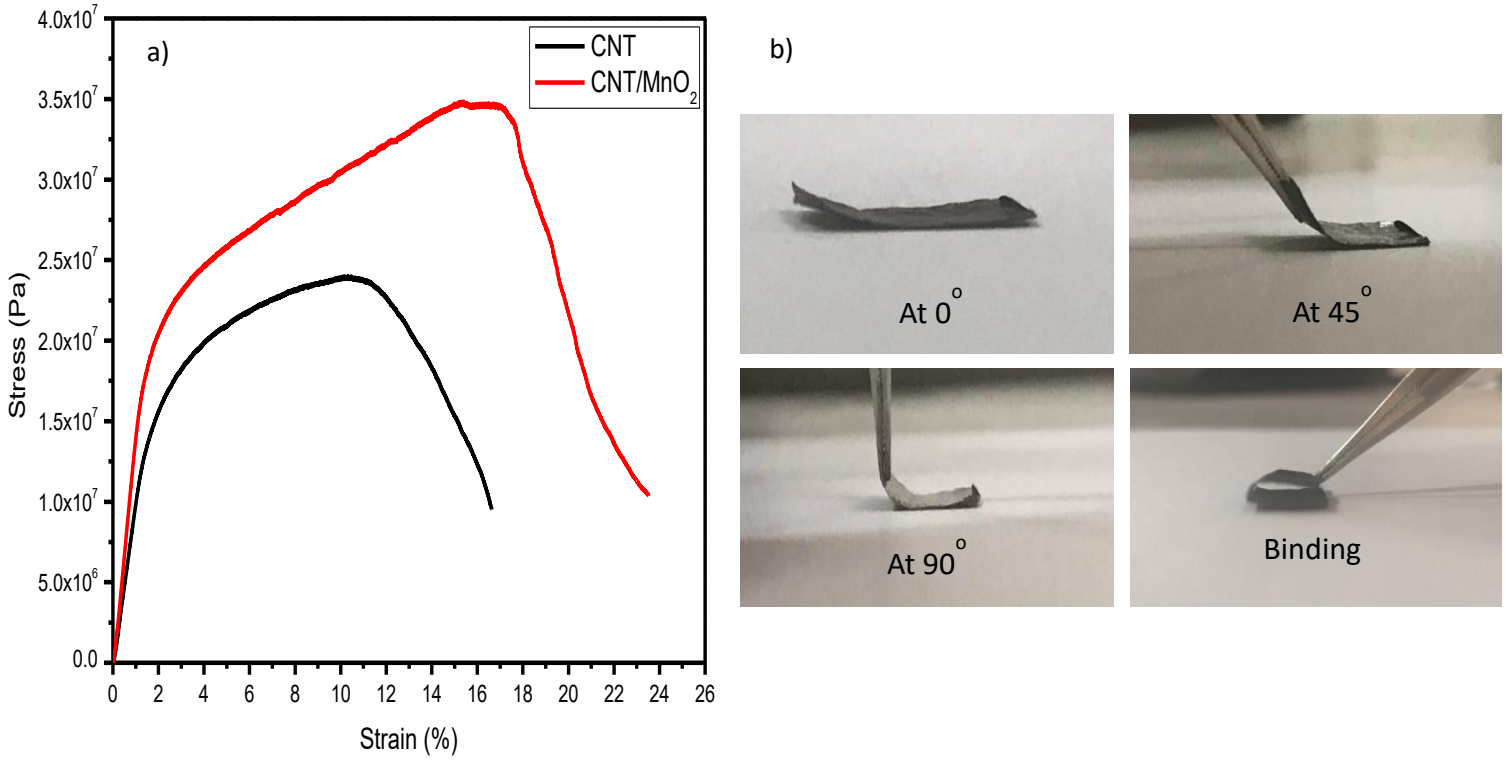

Figure 30. Mechanical characterization of CNTs and CNTs/MnO_2 sample with 1000 nm MnO_2 thickness (a) Tensile test (b) photographs of CNTs/MnO_2 sample at various angles

4.2 Electrochemical Performance

The electrochemical performance of the CNTs/MnO_2 composite as a capacitive energy storage is studied via CV, EIS, and GCD. The composite was examined with 1M Na_2SO_4 electrolyte in the three-electrode cell using SCE as a reference electrode and graphite as a counter electrode at room temperature. Figure 31 illustrates the CV curves of CNTs/MnO_2 samples with different MnO_2 thicknesses. Figures 31a-c, present the effect of the scan rate 5, 10, 50, 100 and 200 mV/s in the potential range between 0 and 1 V/SCE. At small scan rates (5 and 10 mV/s), CV curves of all CNTs/MnO_2 composites display a quasi-rectangle shape without a redox peak, demonstrating pseudocapacitive behavior with fast and reversible surface reactions indicating good capacitive characteristics.[132] Under large scan rate (200 mV/s), CV curves are still symmetrical representing excellent capacitor behaviors for all MnO_2 thicknesses. Additionally, it can be noticed that at 5 mV/s the area of the CV loop of blank CNTs is much smaller than that of CNTs/MnO_2 composite films (Figure 31d) indicating that the specific capacitance is smaller than that of CNTs/MnO_2 composite films. Commonly, at the same scanning rate, the integral area of CV curves is commensurate with specific capacitance. The specific capacitances (Cs) of the CNTs and CNTs/MnO_2 electrodes were measured from their CV curves at various scan rates using the following equation: [133]

$$C_s = \frac{1}{m \times v \times (V_2 - V_1)} \int_{V_1}^{V_2} I(V) dV \qquad (7)$$

where C_s (F/g) is the specific capacitance; m (mg) is the mass of MnO_2; v (V/s) is the scan rate; I (A) is the discharge current; V_2 and V_1 (V) are high and low potential limit of the

CV tests, and $\int_{V_1}^{V_2} I(V)dV$ is the integral area under the CV curve. Using Equation 7, the specific capacitance for CNTs electrode at 5 mV/s was calculated to be 200 F/g which is similar to values previously reported.[134] While, the specific capacitance for the samples with 350, 700 and 1000 nm MnO_2 thickness at same scan rates are 564, 609, and 1676 F/g respectively. Among these, the sample with a MnO_2 thickness of 1000 nm showed the highest capacitance value followed by 700 nm and 350 nm. Hence, it can be speculated that increasing the distance of ionic motion from the electrolyte to the inner MnO_2 in the electrode is necessary. The overall specific capacitances for the sample with 350 nm thick MnO_2 are 564, 463, 230, 160 and 110 F/g at 5, 10, 50, 100 and 200 mV/s, respectively. While, the specific capacitances for the sample with 700 nm thick MnO_2 are 608, 510, 239, 166 and 110 F/g and for the sample with 1000 nm thick MnO_2 are 1676, 1267, 474, 295 and 177 F/g for same scan rates. The higher capacitance than the theoretical value (1370 F/g) (especially for low scan rates) is linked to pseudocapacitance due to reversible redox reactions and not limited to only Mn^{4+}/Mn^{3+} accompanied by the insertion/deinsertion of alkali Na^+ cation or H^+ protons from the electrolyte.[135] Even so, there is no doubt that the as-prepared CNTs/MnO_2 composites films have a good pseudocapacitive behavior.

Figure 31e shows the specific capacitance as a function of the MnO_2 thickness and the scan rate. The specific capacitance decreases with increasing the scan rate because some alkali cations with high scan rates don't have the time to be absorbed on the CNTs/MnO_2 surface.[136]

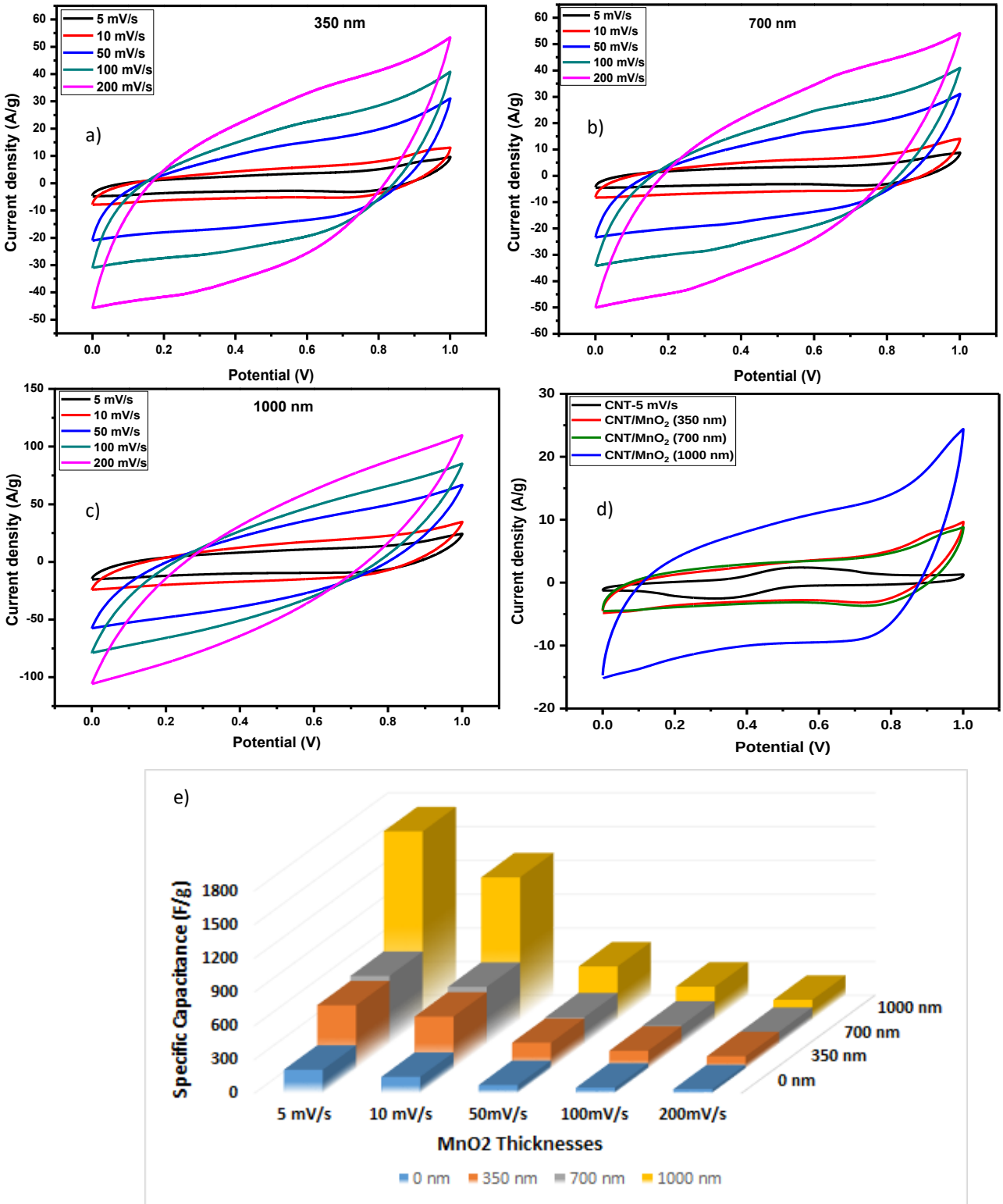

Figure 31. CV curves of CNTs/MnO_2 at different scan rates for samples with (a) 350 nm, (b) 700 nm, (c) 1000 nm MnO_2, (d) CNTs and CNTs/MnO_2 at scan rate of 5 mV/s in 1 M Na_2SO_4 and (e) The dependence of the specific capacitance on electrode film thickness, for various scan rates.

To more understand of the electrochemical behaviors of the electrodes with different MnO_2 thicknesses, EIS measurements were carried out on CNTs and CNTs/MnO_2 films based supercapacitors over a frequency range of 10^5 to 0.0001 Hz with voltage amplitude 100 mV and 20 steps/decade vs SCE reference electrode. Figure 32a presents the Nyquist plots of the CNTs and three different thicknesses of MnO_2 electrodes. It can be seen that a semicircle pattern is observed in all of the electrodes at a mid-high frequency which represents the charge transfer resistance (R_{ct}) processes existing at the electrode/electrolyte interface, and the double layer capacitance.[137] A linear Warburg-type line is detected at a low-frequency range, which is related to the ion diffusion from the electrolyte to the electrode surface.[138] EIS can be fitted by an equivalent circuit shown in the Figure 32c. CNTs film shows small semicircle compared to that of CNTs/MnO_2 films, indicating a higher interfacial charge-transfer resistance for CNTs/MnO_2 films due to the poor electrical conductivity of the MnO_2 material. However, the diameter of the semicircle of the electrode with a thickness of 1000 nm is much lower than that of the electrodes 700 and 350 nm, due to the R_{ct} of the electrode is much larger than that of the other electrodes. This is why a larger pseudocapacitance was obtained for the electrode with 1000 nm MnO_2 thickness at the same scan rates. Besides that, a sharper Warburg impedance for the CNTs/MnO_2 films depicted, indicating that the device has good capacitive behavior with fast ion diffusion. These results demonstrate that the composite has the capability to improve the electrolyte interaction with the active materials and assist the penetration of electrolyte into the MnO_2 surface, presenting a better capacitive performance and pathway for ion diffusion.

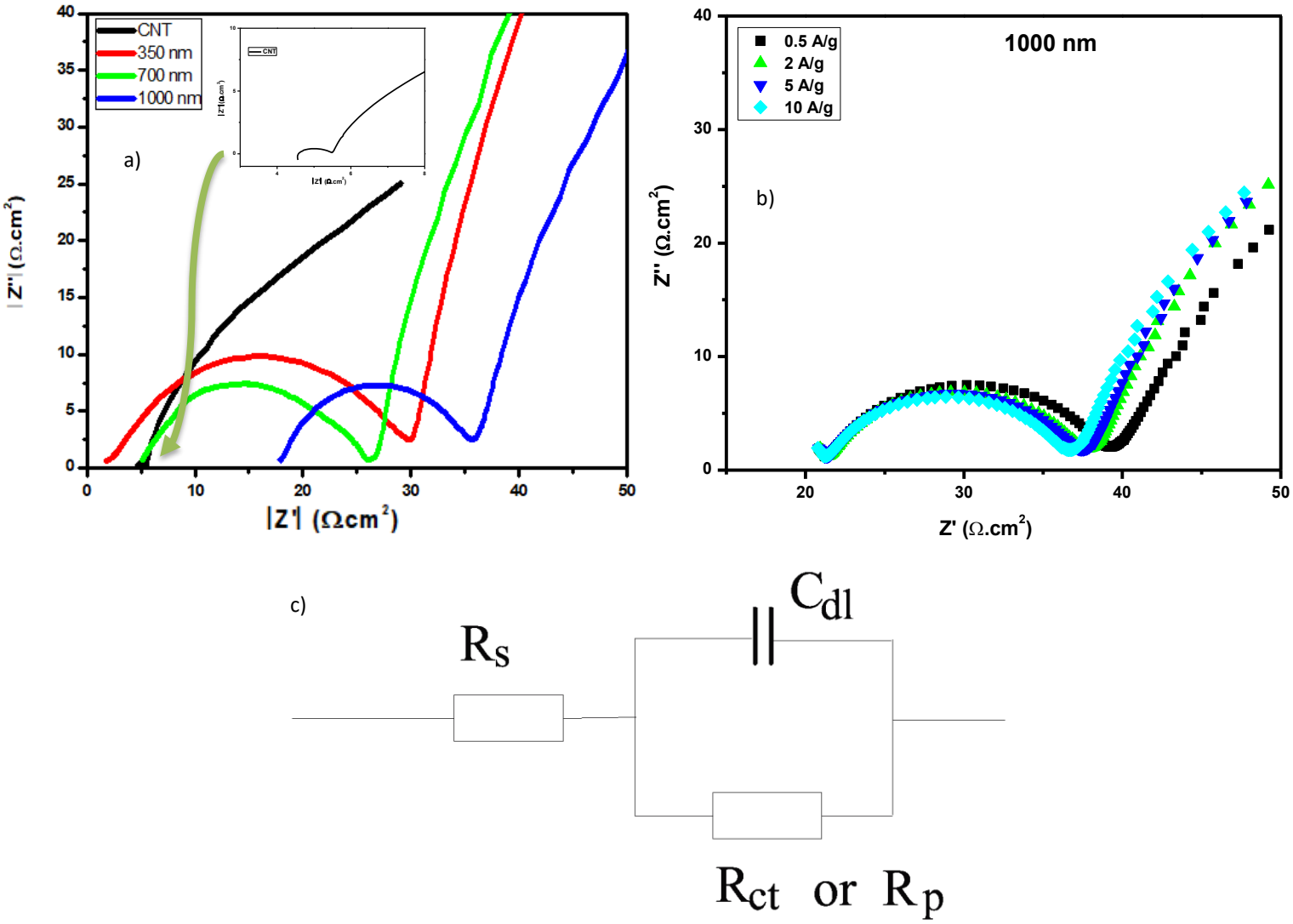

Figure 32. EIS spectra of (a) CNTs and CNTs/MnO_2 electrodes at fresh electrodes (inset the EIS spectra of CNTs), (b) CNTs/MnO_2 electrode with 1000 nm MnO_2 at different current densities and (c) the equivalent circuit.

The GCD curves of the composite films at different current densities 0.5, 1, 2, 5 and 10 A/g are shown in Figure 33a-c. The curves almost symmetric with linear shapes, indicating high specific capacitance and electrochemical activity and matching with the results of CV tests. The specific capacitances (Cs) of the CNTs and CNTs/MnO_2 electrodes in three electrode configuration were derived from their galvanostatic charge/discharge curves at various current densities using the following equation: [120]

$$C = \frac{I.\Delta t}{m.\Delta V} \qquad (8)$$

where I represents the discharging or charging current, t is the discharge or charging time, ΔV is equal to 1.0 V is the potential window of cycling, and m is the mass of MnO_2. Using Equation 8, the specific capacitance for CNTs electrode at 0.5 A/g was calculated to be 191 F/g. While, according to MnO_2 weight calculation, the specific capacitances of CNTs/MnO_2 for 350 nm was 1600 F/g, for 700 nm was 3200 F/g and for 1000 nm was 6364 F/g at a small current density of 0.5 A/g. Figure 33d shows that as MnO_2 loading on the surface of CNTs increases, the specific capacitance increased.

Furthermore, the specific capacitance with charging−discharging cycle numbers at 2 A/g from 0 to 1 V for 400 cycles in 1 M Na_2SO_4 aqueous solution is shown in Figure 34a. It is clear that the pristine CNTs demonstrates better cyclic stability than the composites CNTs/MnO_2 with only 16% degradation. Although, the specific capacitance of the composites is much higher than that of the CNTs. Figure 34b, CNTs/MnO_2 electrode with 1000 nm thickness exhibits highest specific capacitance and cyclic stability with capacitance retention of 85.8% of its peak value after 400 cycles. While after the same

cycles the composite of 700 nm exposed 40% decay from the initial capacitance followed by 41% fading for the capacitance of 350 nm thickness as shown in Figure 35. The reason for the huge decay goes back to the dissolution of MnO_2 active material assigned to the disproportionate reaction, which mainly leads to fast performance declining during cycling.[139,140]

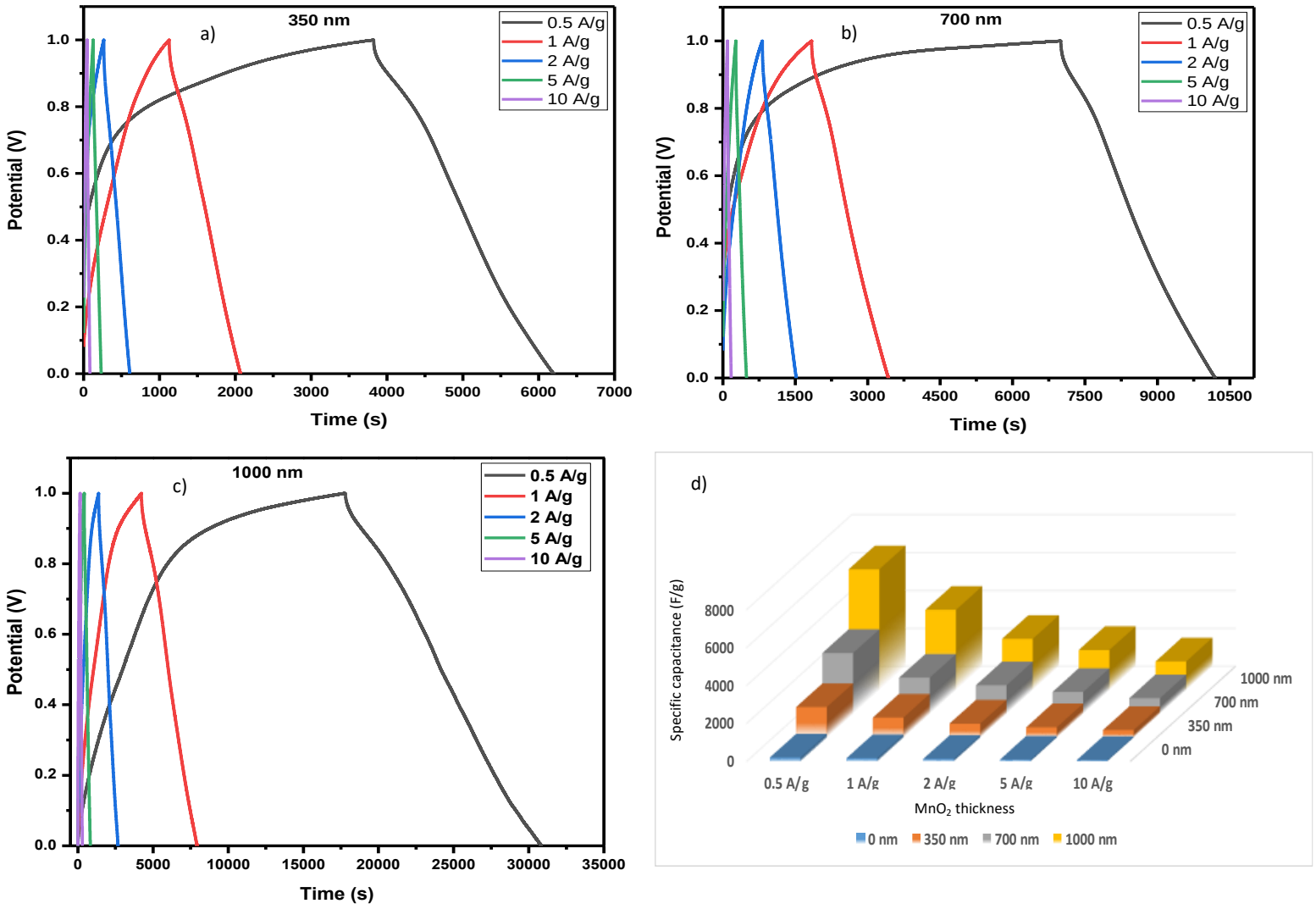

Figure 33. GCD curves of charge/discharge at different current densities for a) 350 nm, b) 700 nm, c) 1000 nm MnO_2 thickness, d) specific capacitance vs MnO_2 thickness for three electrodes.

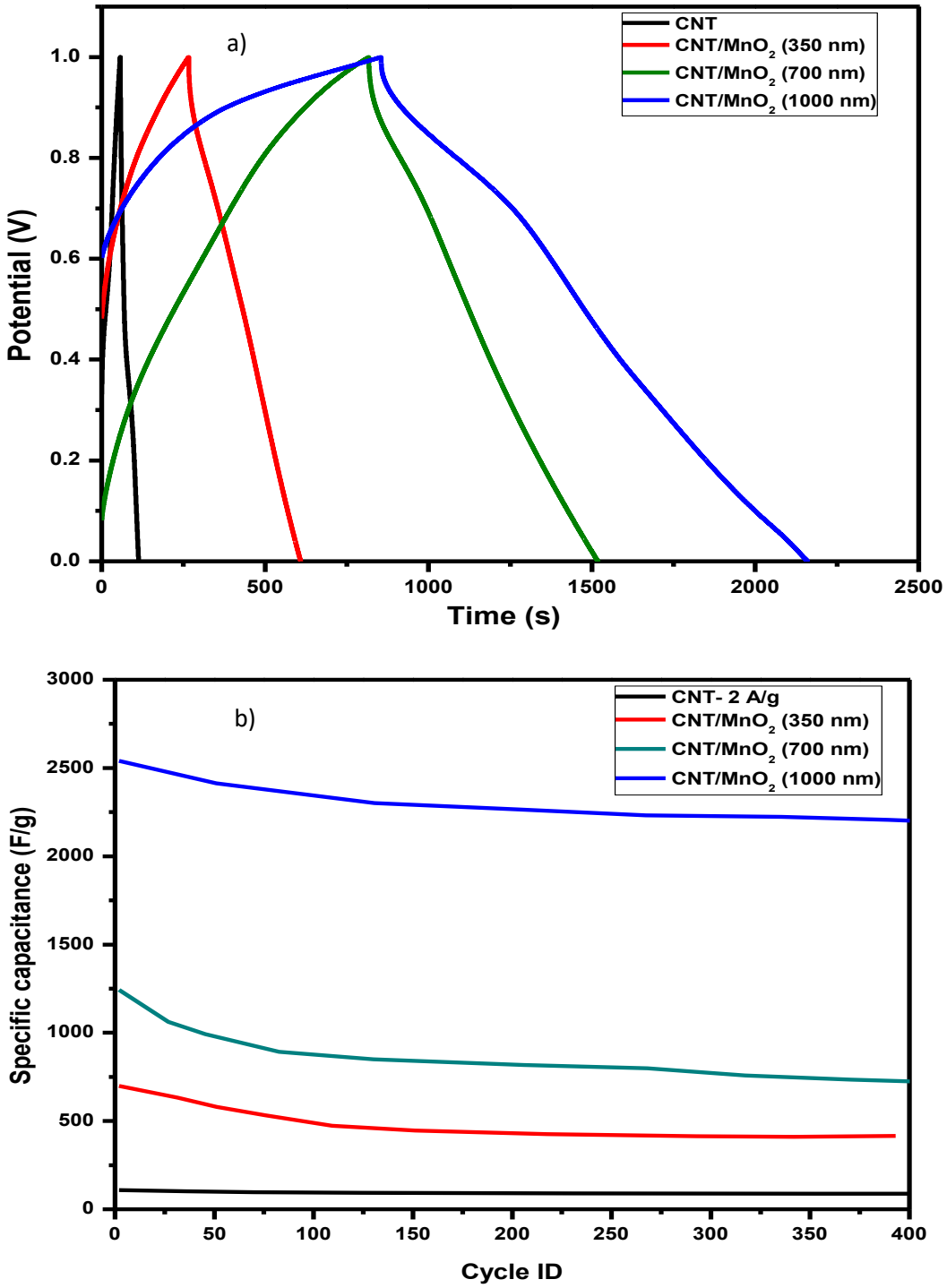

Figure 34. GCD test presenting a) charge/discharge and b) Cycling performance of CNTs and CNTs/MnO_2 at 2 A/g in 1 M Na_2SO_4 after 400 cycles.

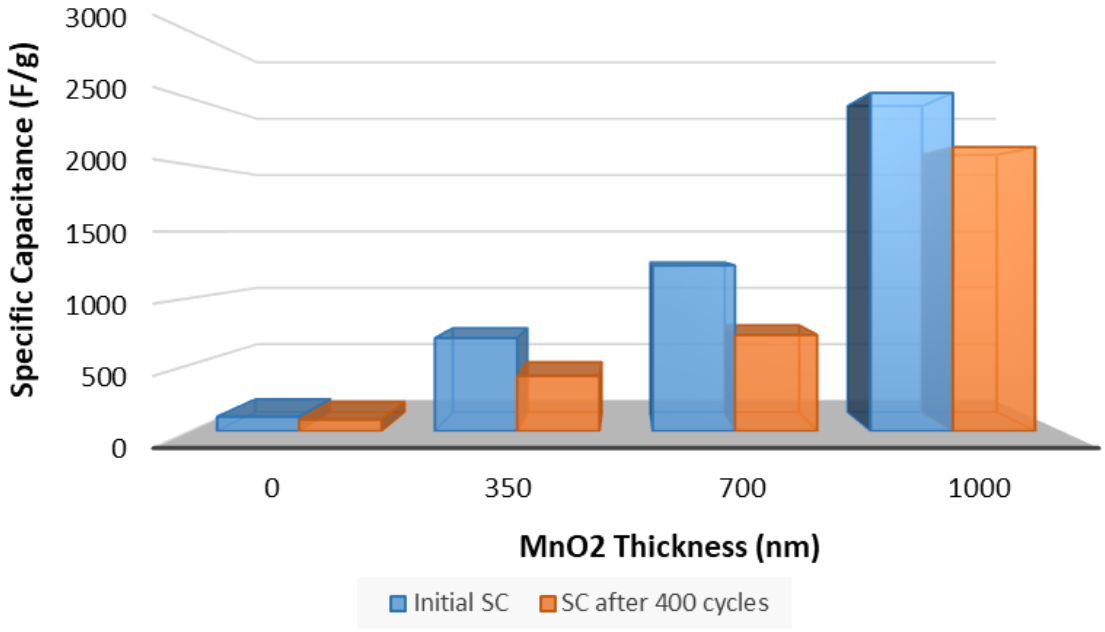

Figure 35. The bar chart shows the change of specific capacitance before and after 400 cycles

The electrochemical properties of the electrodes with one individual electrode were demonstrated in Figure 36. The symmetric all solid state flexible supercapacitor was prepared by assembling two identical CNTs/MnO_2 fabrics separated with PVA-H_3PO_4 gel and connected with copper foils to assure the electric collection. Re-calling Formula 5 that was used to determine the specific capacitance from the charge-discharge curves in two electrodes symmetric cell configuration:

$$SC= 2(\frac{I.\Delta t}{m.\Delta V})$$

where I represents the constant discharge or discharge current, Δt is the discharging or charging time, m is the mass of MnO_2, and ΔV is equal to 0.8 V is the potential window of cycling. The discharge-specific capacitance values and charge-discharge efficiency for the three symmetric all solid supercapacitor at 2 A/g are presented in Figure 36a-c. The discharge-specific capacitance of the CNTs/MnO_2 electrode with 1000 nm thickness is larger than the other two composite electrodes started with 140 F/g. While the CNTs/MnO_2 electrode with 700 nm exhibits a specific capacitance of 120 F/g and the SC value for the electrode CNTs/MnO_2 electrode with 350 nm thickness is less than 90 F/g. The obtained results show that CNTs/MnO_2 considerably increases the specific capacitance. The difference between the electrodes 350 nm, 700 nm and 1000 nm in the capacitance behavior is associated with the thickness of the MnO_2 film. However, the stability of the electrodes studied after 400 cycles and found the specific capacitance of CNTs/MnO_2 electrode with 1000 nm thickness decreased by 40% decay of its initial capacitance, while the electrode with 700 nm thickness exhibited 33% decay of its initial capacitance.

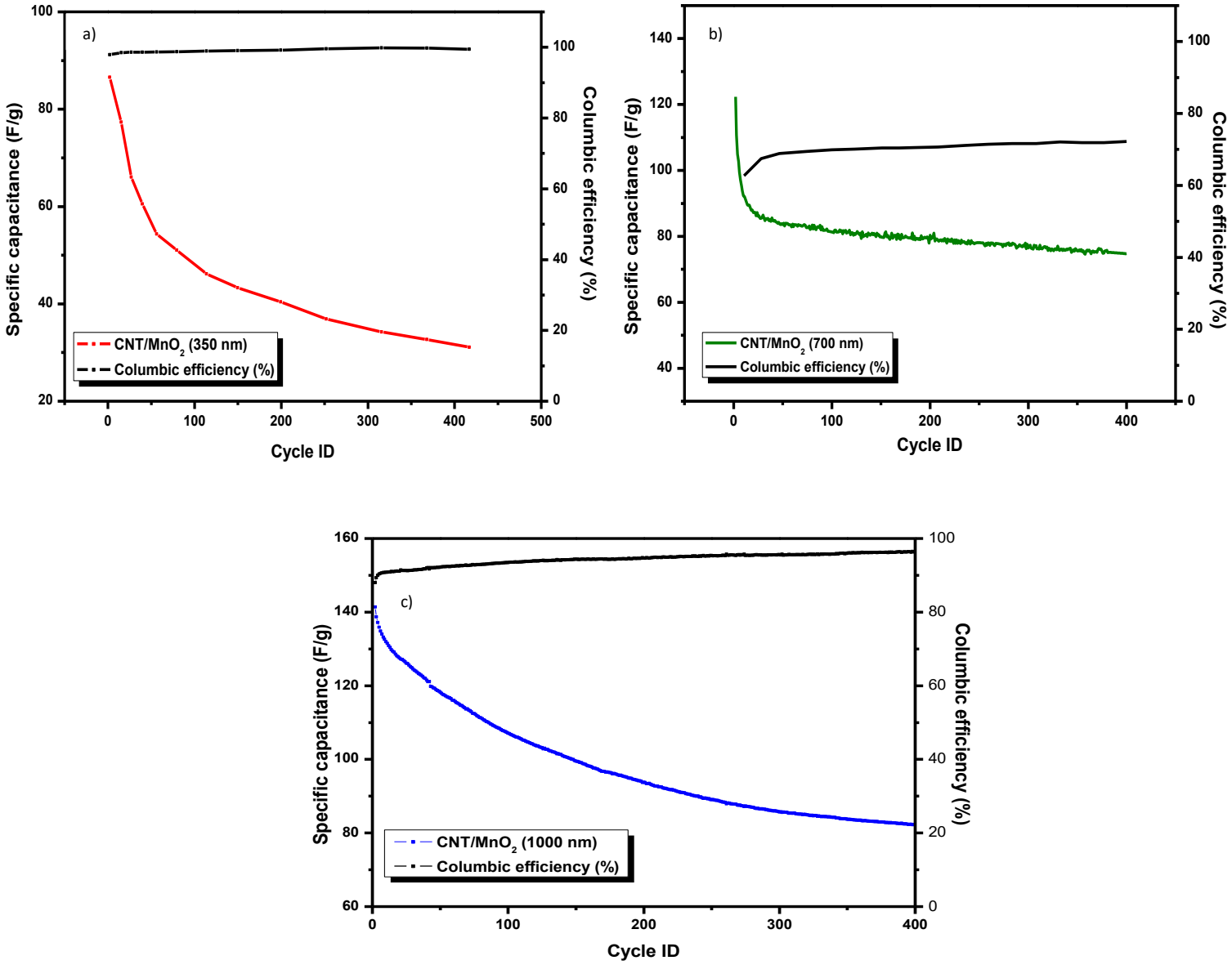

Figure 36. The discharge specific capacitance values and charge-discharge efficiency for CNTs/MnO_2 at (a) 350 nm, (b) 700 nm and (c) 1000 nm symmetric all solid state supercapacitors at 2 A/g.

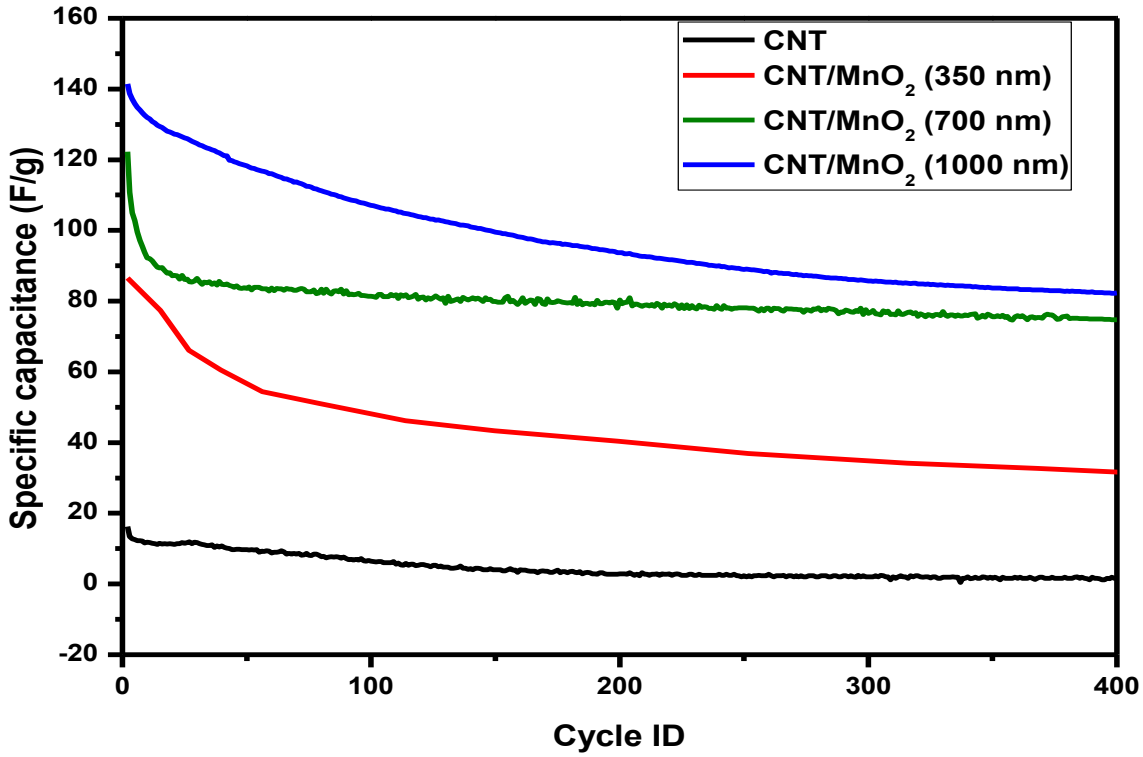

Figure 37. Cycling performance of CNTs and three different thicknesses of flexible all solid CNTs/MnO_2 symmetric supercapacitor at current density 2 A/g.

CHAPTER 5: CONCLUSION

CNTs/MnO_2 composites were successfully fabricated using RF magnetron sputtering deposition of MnO_2 for the first time. CNTs/MnO_2 composite electrodes with three different MnO_2 thicknesses (300, 700, 1000 nm) were prepared, characterized and compared with pure CNTs sheet. Different characterization techniques were conducted to study their properties. Surface morphology studied by SEM images that demonstrated, a uniform and homogenous MnO_2 layers structural. XPS, XRD, and Raman spectroscopy measurements confirmed the existence of MnO_2 films on the CNTs surface. In addition, stress-strain curves displayed the mechanical properties and the flexibility of the prepared CNTs/MnO_2 composite electrodes with 1000 nm MnO_2 thick compared with CNTs sheet.

The electrochemical behavior of the CNTs/MnO_2 composites was investigated in three electrodes starting with the thin electrode with 350 nm, medium electrode with 700 nm and a thick electrode with 1000 nm MnO_2 thickness in 1M of Na_2SO_4 via cyclic voltammetry (CV), electrochemical impedance spectroscopy (EIS), and galvanostatic charge/discharge (GCD). The CV curves and GCD test displayed that all electrodes with different MnO_2 thicknesses showed excellent pseudocapacitive behavior as compared with CNTs sheet with high specific capacitance reached to 1676 F/g under small scan rates of 1000 nm MnO_2 thickness followed with 700 nm and 350 nm MnO_2 thickness.

Furthermore, the electrode with 1000 nm MnO_2 thickness displayed a good cyclic stability with capacitance retention of 85.8% of its peak value after 400 cycles and approximately 41% degradation of the capacitance for the other two electrodes.

In a two-electrode system producing all solid-state flexible supercapacitor with a PVA/H_3PO_4/CNTs/MnO_2 symmetric capacitor, the specific capacitance of the electrodes

with 1000 nm MnO_2 thickness showed the highest capacitance among the other electrodes. Among all the thickness, the electrode with 700 nm thickness of MnO_2 exhibited the highest cyclic stability with 33% decay of its initial capacitance after 400 cycles.

All the results of CNTs/MnO_2 proved that this technique could be used with further enhancements for applications in an electrochemical supercapacitor and it is evidenced as the thickness increases, the specific capacitance increases, indicating that the utilization of MnO_2 became more efficient in the electrodes and present great pseudocapacitive behavior.

Our calculation of the active material is based on the weight of MnO_2 only. In the literature review, the reported values of the capacitance are based on the weight of CNTs and MnO_2. This will not allow for us to make a fair comparison between our findings and the literature review.

FUTURE WORK

Supercapacitors are attracting a lot of interest. These units, designed to store energy, with their ability to create rapid charging discharging as well as their large power density. In future work, we may change the sputtering conditions to improve the surface morphology and structure of the MnO_2 films deposited on CNTs. It would be interesting to anneal Mno2/ CNTs at different temperatures and study their effect on the performance of the device. Finally, it is important to test the all solid-state supercapacitor stability for longer life cycles.

REFERENCES

1 G. P. Wang, L. Zhang and J. J. Zhang, *Chem. Soc. Rev.*, 2012, **41**, 797–828.

2 R. a. Fisher, M. R. Watt, W. Jud Ready, S. Il Cho, Z. Chen, D. Yang and H. Lu, *Energy Environ. Sci.*, 2013, **3**, 4889–4899.

3 Z. Fan, J. Yan, T. Wei, L. Zhi, G. Ning, T. Li and F. Wei, *Adv. Funct. Mater.*, 2011, **21**, 2366–2375.

4 Y. Zhu, S. Murali, M. D. Stoller, K. J. Ganesh, W. Cai, P. J. Ferreira, A. Pirkle, R. M. Wallace, K. A. Cychosz, M. Thommes, D. Su, E. A. Stach and R. S. Ruoff, *Chem. Soc. Rev.*, 2011, **332**, 1537–1542.

5 J. Cao, Y. Wang, Y. Zhou, J. Ouyang, D. Jia and L. Guo, *J. Electroanal. Chem.*, 2013, **689**, 201–206.

6 L. T. Le, M. H. Ervin, H. Qiu, B. E. Fuchs and W. Y. Lee, *Electrochem. commun.*, 2011, **13**, 355–358.

7 Y. Xie, Y. Liu, Y. Zhao, Y. H. Tsang, S. P. Lau, H. Huang and Y. Chai, *J. Mater. Chem. A*, 2014, 9142–9149.

8 E. J. Ra, E. Raymundo-Piñero, Y. H. Lee and F. Béguin, *Carbon N. Y.*, 2009, **47**, 2984–2992.

9 C. Kim and K. S. Yang, *Appl. Phys. Lett.*, 2003, **1216**, 9–12.

10 F. H. Gojny, J. Nastalczyk, Z. Roslaniec and K. Schulte, *Chem. Phys. Lett.*, 2003, 820–824.

11 M. Zhi, C. Xiang, J. Li, M. Li and N. Wu, *Nanoscale*, 2013, 72–88.

12 V. Augustyn, P. Simon and B. Dunn, *Energy Environ. Sci.*, 2014, **7**, 1597.

13 B. Conway, *Springer Sci. Bus. Media*, 1999, 698.

14 A. G. Pandolfo and A. F. Hollenkamp, *J. Power Sources*, 2006, **157**, 11–27.

15 L. L. Zhang, R. Zhou and X. S. Zhao, *J. Mater. Chem.*, 2009, **38**, 2520–2531.

16 A. J. Hone, B. Batlogg, Z. Benes, A. T. Johnson and J. E. Fischer, *Am. Assoc. Adv. Sci. Stable*, 2016, **289**, 1730–1733.

17 E. W. Wong, P. E. Sheehan and C. M. Liebert, *Am. Assoc. Adv. Sci. Stable*, 2016, **277**, 1971–1975.

18 S. J. Tans, A. R. M. Verschueren and C. Dekker, *Nature*, 1998, **672**, 669–672.

19 K. Kerdnawee, C. Termvidchakorn, P. Yaisanga, J. Pakchamsai, C. Chookiat, A. Eiad-ua, W. Wongwiriyapan, W. Chaiwat, S. Ratchahat, K. Faungnawakij, K. Suttiponparnit and T. Charinpanitkul, *KONA Powder Part. J.*

20 R. A. Fisher, M. R. Watt and W. J. Ready, 2013, **2**, 3170–3177.

21 P. . b Simon and Y. . Gogotsi, *Nat. Mater.*, 2008, **7**, 845–854.

22 W. Deng, X. Ji and C. E. Banks, *RSC Adv.*, 2011, 1171–1178.

23 X. Xia, J. Tu, Y. Mai, X. Wang, C. Gu and X. Zhao, *J. Mater. Chem.*, 2011, **21**, 9319.

24 S. K. Meher and G. R. Rao, *J. Phys. Chem. C*, 2011, **115**, 15646–15654.

25 L. Demarconnay, E. Raymundo-Piñero and F. Béguin, *J. Power Sources*, 2011, **196**, 580–586.

26 G. Yu, L. Hu, N. Liu, H. Wang, M. Vosgueritchian, Y. Yang, Y. Cui and Z. Bao, *Nano Lett.*, 2011, **11**, 4438–4442.

27 H. Xia, Y. Shirley Meng, G. Yuan, C. Cui and L. Lu, *Electrochem. Solid-State Lett.*, 2012, **15**, A60.

28 C. C. Hu, K. H. Chang, M. C. Lin and Y. T. Wu, *Nano Lett.*, 2006, **6**, 2690–2695.

29 T. Liu, W. G. Pell and B. E. Conway, *Electrochim. Acta*, 1997, **42**, 3541–3552.

30 K. S. Ryu, K. M. Kim, N. G. Park, Y. J. Park and S. H. Chang, *J. Power Sources*, 2002, **103**, 305–309.

31 G. A. Snook, P. Kao and A. S. Best, *J. Power Sources*, 2011, **196**, 1–12.

32 E. Frackowiak, V. Khomenko, K. Jurewicz, K. Lota and F. Béguin, *J. Power Sources*, 2006, **153**, 413–418.

33 M. Mastragostino, M. Mastragostino, C. Arbizzani and F. Soavi, *Solid State Ionics*, 2002, **148**, 493–498.

34 L. Li, Z. A. Hu, N. An, Y. Y. Yang, Z. M. Li and H. Y. Wu, *J. Phys. Chem. C*, 2014, **118**, 22865–22872.

35 A. Burke, *J. Power Sources*, 2000, 37–50.

36 A. K. Shukla, S. Sampath and K. and Vijayamohanan, *Curr. Sci. Assoc.*, 2000, **79**, 1656–1661.

37 H. Li, X. Zhang, R. Ding, L. Qi and H. Wang, *Electrochim. Acta*, 2013, **108**, 497–505.

38 H. Wang, C. Peng, J. Zheng, F. Peng and H. Yu, *Mater. Res. Bull.*, 2013, **48**, 3389–3393.

39 M. Toupin, T. Brousse and D. Be, *Chem. Mater.*, 2004, 3184–3190.

40 M. R. Bailey and S. W. Donne, *Electrochem. Soc.*, 2012, **159**, 3–8.

41 B. E. Conway, *Kluwer Acad. Press*, , DOI:10.1002/9783527639496.ch8.

42 L. L. Zhang and X. S. Zhao, *Chem. Soc. Rev.*, 2009, **38**, 2520.

43 S. Chen, J. Zhu, X. Wu, Q. Han and X. Wang, *Am. Chem. Soc.*, 2010, **4**, 2822–2830.

44 Y. Hou, Y. Cheng, T. Hobson and J. Liu, *Nano Lett.*, 2010, **10**, 2727–2733.

45 R. N. Reddy and R. G. Reddy, *J. Power Source*, 2003, **124**, 330–337.

46 E. M. Jin, J. G. Lim and S. M. Jeong, *J. Ind. Eng. Chem.*, 2017, **54**, 421–427.

47 J. Liu, J. Essner and J. Li, *Chem. Mater.*, 2010, **104**, 5022–5030.

48 J. Gomez and E. E. Kalu, *J. Power Sources*, 2013, **230**, 218–224.

49 J. N. Tiwari, R. N. Tiwari and K. S. Kim, *Prog. Mater. Sci.*, 2012, **57**, 724–803.

50 M. A. Pope, S. Korkut, C. Punckt and I. A. Aksay, *J. Electrochem. Soc.*, 2013, **160**, A1653–A1660.

51 J. S. Zheng, L. Zhang, A. Shellikeri, W. Cao, Q. Wu and J. P. Zheng, *Sci. Rep.*, 2017, **7**, 1–8.

52 J. A. Ocampo, *Ind. Dev. 21st Century Sustain. Dev. Perspect.*, 2007, 1–4.

53 S. Devaraj and N. Munichandraiah, *Electrochem. Solid-State Lett.*, 2005, **8**, A373.

54 J. Yan, Z. Fan, T. Wei, W. Qian, M. Zhang and F. Wei, *Carbon N. Y.*, 2010, **48**, 3825–3833.

55 Y. Wang, Y. Liu and I. Zhitomirsky, *J. Mater. Chem. A*, 2013, **1**, 12519.

56 Q. Cheng, J. Tang, J. Ma, H. Zhang, N. Shinya and L. C. Qin, *Carbon N. Y.*, 2011, **49**, 2917–2925.

57 J. Yan, Z. Fan, T. Wei, J. Cheng, B. Shao, K. Wang, L. Song and M. Zhang, *J. Power Sources*, 2009, **194**, 1202–1207.

58 D. Ganguly, D. Pahari, N. S. Das, P. Howli, B. Das, D. Banerjee and K. K. Chattopadhyay, *J. Electroanal. Chem.*, 2016, **778**, 12–22.

59 R.-R. Bi, Y.-X. Yin, Y.-G. Guo and L.-J. Wan, *J. Nanosci. Nanotechnol.*, 2011, **11**, 1996–2002.

60 A. L. M. Reddy, M. M. Shaijumon, S. R. Gowda and P. M. Ajayan, *J. Phys. Chem. C*, 2010, **114**, 658–663.

61 S. Kalathil, V. H. Nguyen, J.-J. Shim, M. M. Khan, J. Lee and M. H. Cho, *J. Nanosci. Nanotechnol.*, 2013, **13**, 7712–7716.

62 W. Xiao, H. Xia, J. Y. H. Fuh and L. Lu, *Phys. Scr. T*.

63 T. Bordjiba and D. Bélanger, *Electrochim. Acta*, 2010, **55**, 3428–3433.

64 T. H. Lee, D. T. Pham, R. Sahoo, J. Seok, T. H. T. Luu and Y. H. Lee, *Energy Storage Mater.*, 2018, **12**, 223–231.

65 B. Patil, S. Ahn, C. Park, H. Song, Y. Jeong and H. Ahn, *Energy*, 2018, **142**, 608–616.

66 W. Qi, X. Li, Y. Wu, H. Zeng, C. Kuang, S. Zhou, S. Huang and Z. Yang, *Surf. Coatings Technol.*, 2017, **320**, 624–629.

67 N. R. Chodankar, S. H. Ji and D. H. Kim, *J. Taiwan Inst. Chem. Eng.*, 2017, **80**, 503–510.

68 D. Gueon and J. H. Moon, *ACS Sustain. Chem. Eng.*, 2017, **5**, 2445–2453.

69 Y. Zhao, M. P. Li, S. Liu and M. F. Islam, *ACS Appl. Mater. Interfaces*, 2017, **9**, 23810–23819.

70 H. Huang, W. Zhang, Y. Fu and X. Wang, *Electrochim. Acta*, 2015, **152**, 480–488.

71 H. Wang, C. Peng, F. Peng, H. Yu and J. Yang, *Mater. Sci. Eng. B Solid-State Mater. Adv. Technol.*, 2011, **176**, 1073–1078.

72 L. Hu, W. Chen, X. Xie, N. Liu and Y. Yang, *ACS Nano*, 2011, 8904–8913.

73 X. Jin, W. Zhou, S. Zhang and G. Z. Chen, *Small*, 2007, **3**, 1513–1517.

74 S. W. Lee, J. Kim, S. Chen, P. T. Hammond and Y. Shao-Horn, *ACS Nano*, 2010, **4**, 3889–3896.

75 S. L. Chou, J. Z. Wang, S. Y. Chew, H. K. Liu and S. X. Dou, *Electrochem. commun.*, 2008, **10**, 1724–1727.

76 V. Subotić, C. Schluckner, J. Strasser, V. Lawlor, J. Mathe, J. Rechberger, H. Schroettner and C. Hochenauer, *Electrochim. Acta*, 2016, **207**, 224–236.

77 R. Holze and J. Lippe, *Synth. Met.*, 1990, **38**, 99–105.

78 S. Akbulut, M. Yilmaz, S. Raina, S. H. Hsu and W. P. Kang, *Diam. Relat. Mater.*, 2017, **74**, 222–228.

79 W. Liu, S. Wang, Q. Wu, L. Huan, X. Zhang, C. Yao and M. Chen, *Chem. Eng. Sci.*, 2016, **156**, 178–185.

80 J. Chen, Y. Huang, X. Zhang, X. Chen and C. Li, *Ceram. Int.*, 2015, **41**, 12680–12685.

81 X. Xie and L. Gao, *Carbon N. Y.*, 2007, **45**, 2365–2373.

82 M. Yoshimura and K. Byrappa, *J. Mater. Sci.*, 2008, **43**, 2085–2103.

83 K. Byrappa and T. Adschiri, *Prog. Cryst. Growth Charact. Mater.*, 2007, **53**, 117–166.

84 T. Cheng, B. Yu, L. Cao, H. Tan, X. Li, X. Zheng, W. Li, Z. Ren and J. Bai, *J. Colloid Interface Sci.*, 2017, **501**, 1–10.

85 P. A. Shinde, V. C. Lokhande, T. Ji and C. D. Lokhande, *J. Colloid Interface Sci.*, 2017, **498**, 202–209.

86 X. Luo, J. Yang, D. Yan, W. Wang, X. Wu and Z. Zhu, *J. Alloys Compd.*, 2017, **723**, 505–511.

87 J. Livage, M. Henry and C. Sanchez, *Prog. Solid State Chem.*, 1988, **18**, 259–341.

88 S. Mann, S. L. Burkett, S. A. Davis, C. E. Fowler, N. H. Mendelson, S. D. Sims, D. Walsh and N. T. Whilton, *Chem. Mater.*, 1997, **9**, 2300–2310.

89 S. Licoccia, R. Polini, C. D'Ottavi, F. S. Fiory, M. L. Di Vona and E. Traversa, *J. Nanosci. Nanotechnol.*, 2005, **5**, 592–595.

90 M. Chem, F. Jabeen and M. S. Nawaz, *Mod. Chem. Appl.*, 2016, **4**, 1–7.

91 A. Vioux, *Chem. Mater.*, 1997, **9**, 2292–2299.

92 R. N. Reddy and R. G. Reddy, *J. Power Sources*, 2004, **132**, 315–320.

93 A. Darari, H. R. Ardiansah, A. Arifin, N. Rismaningsih, A. N. Ningrum and A. Subagio, *AIP Conf. Proc.*

94 H. N. Alshareef, W. Chen, R. B. Rakhi, L. Hu, X. Xie and Y. Cui, *Nano Lett.*, 2011, **11**, 5165–5172.

95 C. Guo, H. Li, X. Zhang, H. Huo and C. Xu, *Sensors Actuators, B Chem.*, 2015, **206**, 407–414.

96 L. Li, Z. A. Hu, N. An, Y. Y. Yang, Z. M. Li and H. Y. Wu, *J. Phys. Chem. C*, 2014, **118**, 22865–

22872.

97 G. Wang, X. Sun, F. Lu, H. Sun, M. Yu, W. Jiang, C. Liu and J. Lian, *Small*, 2012, **8**, 452–459.

98 Z. Weng, Y. Su, D. W. Wang, F. Li, J. Du and H. M. Cheng, *Adv. Energy Mater.*, 2011, **1**, 917–922.

99 S. Zhang, Y. Li and N. Pan, *J. Power Sources*, 2012, **206**, 476–482.

100 Y. Wang, J. Chen, J. Cao, Y. Liu, Y. Zhou, J. H. Ouyang and D. Jia, *J. Power Sources*, 2014, **271**, 269–277.

101 P. Wu, S. Cheng, L. Yang, Z. Lin, X. Gui, X. Ou, J. Zhou, M. Yao, M. Wang, Y. Zhu and M. Liu, *ACS Appl. Mater. Interfaces*, 2016, **8**, 23721–23728.

102 J. Milne and I. Zhitomirsky, *J. Colloid Interface Sci.*, 2018, **515**, 50–57.

103 R. Chen, R. Poon, R. P. Sahu, I. K. Puri and I. Zhitomirsky, *J. Electrochem. Soc.*, 2017, **164**, A1673–A1678.

104 R. López-Chavéz and A. K. Cuentas-Gallegos, *J. New Mater. Electrochem. Syst.*, 2013, **16**, 197–202.

105 N. Syarif, I. Tribidasari and W. Wibowo, *J. Electrochem. Sci. Eng.*, 2013, **3**, 37–45.

106 F. Ataherian, Y. Wang, A. Tabet-Aoul and M. Mohamedi, *ChemElectroChem*, 2017, **4**, 1924–1931.

107 K. Evanoff, J. Benson, M. Schauer, I. Kovalenko, D. Lashmore, W. J. Ready and G. Yushin, *ACS Nano*, 2012, **6**, 9837–9845.

108 A. Prakash, University of Central Florida, 2016.

109 D. R. Gibson, I. Brinkley, E. Waddell and J. M. Walls, *Proc. SPIE*, 2008, **7101**, 710108.

110 E. Pascual, E. Martı, J. Esteve and A. Lousa, *Diam. Relat. Mater.*, 1999, **8**, 402–405.

111 A. Kossoy, R. L. Magnusson, T. K. Tryggvason, K. Leosson and S. Olafsson, *J. Vac. Sci.*

Technol. A Vacuum, Surfaces, Film., 2015, **33**, 021514.

112 T. Lohner, M. Serényi, D. K. Basa, N. Q. Khánh, Á. Nemcsics, P. Petrik and P. Turmezei, *Acta Polytech. Hungarica*, 2008, **5**, 23–30.

113 R. R. Cowden, *Scanning Electron Microscopy and X-Ray Microanalysis*, Wiley on behalf of American Microscopical Society Stable, 1983, vol. 102.

114 L. S. Price, I. P. Parkin, A. M. E. Hardy, R. J. H. Clark, T. G. Hibbert and K. C. Molloy, *Chem. Mater.*, 1999, **11**, 1792–1799.

115 D. M. Berg, M. Arasimowicz, R. Djemour, L. Gütay, S. Siebentritt, S. Schorr, X. Fontané, V. Izquierdo-Roca, A. Pérez-Rodriguez and P. J. Dale, *Thin Solid Films*, 2014, **569**, 113–123.

116 D. Briggs and M. Seah, *Practical surface analysis*, Chichester, 2nd edn., 1990, vol. 1.

117 Y. Chen, A. H. Clausen, O. S. Hopperstad and M. Langseth, *Int. J. Solids Struct.*, 2009, **46**, 3825–3835.

118 H. Bjerkaas, *Hans Bjerkaas Characterisation and Plasticity in Extruded Al-Mg-Si Profiles engaging In-situ EBSD Thesis for the degree philosophiae doctor*, 2007.

119 E. Guittet, A. I. Aria, P. M. Gharib and J. Pr, California Institute of Technology, 2011.

120 H. Wang, H. Yi, X. Chen and X. Wang, 2013, **200092**, 1–10.

121 M. Dornajafi, University of Maryland, 2010.

122 P. Martin, 2017, 1–12.

123 L. Zhang, J. Yang, X. Wang, B. Zhao and G. Zheng, *Nanoscale Res. Lett.*, 2014, **9**, 1–8.

124 L. Li, K. H. Seng, Z. Chen, Z. Guo and H. K. Liu, *Nanoscale*, 2013, **5**, 1922.

125 A. Ogata, S. Komaba, R. Baddour-Hadjean, J. P. Pereira-Ramos and N. Kumagai, *Electrochim. Acta*, 2008, **53**, 3084–3093.

126 M. A. Salam and R. Burk, *Arab. J. Chem.*, 2017, **10**, S921–S927.

127 X. Y. Liu, M. Huang, H. L. Ma, Z. Q. Zhang, J. M. Gao, Y. L. Zhu, X. J. Han and X. Y. Guo, *Molecules*, 2010, **15**, 7188–7196.

128 A. Zahoor, J. S. Jeon, H. S. Jang, M. Christy, Y. Hwang and K. S. Nahm, *Sci. Adv. Mater.*, 2014, **6**, 2712–2723.

129 G. Zhu, Z. He, J. Chen, J. Zhao, X. Feng, Y. Ma, Q. Fan, L. Wang and W. Huang, *Nanoscale*, 2014, **6**, 1079–1085.

130 M. Toupin, T. Brousse and D. Bélanger, *Chem. Mater.*, 2004, **16**, 3184–3190.

131 A. Magee, L. Ladani, T. D. Topping and E. J. Lavernia, *Acta Mater.*, 2012, **60**, 5838–5849.

132 K. Jurewicz, C. Vix-Guterl, E. Frackowiak, S. Saadallah, M. Reda, J. Parmentier, J. Patarin and F. Béguin, *J. Phys. Chem. Solids*, 2004, **65**, 287–293.

133 L. Cao, F. Xu, Y. Y. Liang and H. L. Li, *Adv. Mater.*, 2004, **16**, 1853–1857.

134 K. H. An, W. S. Kim, Y. S. Park, H. J. Jeong, Y. C. Choi, J. M. Moon, D. J. Bae, S. C. Lim and Y. H. Lee, *AIP Conf. Proc.*, 2001, **590**, 241–244.

135 M. J. Young, M. Neuber, A. C. Cavanagh, H. Sun, C. B. Musgrave and S. M. George, *J. Electrochem. Soc.*, 2015, **162**, A2753–A2761.

136 C. Wan, L. Yuan and H. Shen, *Int. J. Electrochem. Sci.*, 2014, **9**, 4024–4038.

137 S. Devaraj and N. Munichandraiah, *J. Electrochem. Soc.*, 2007, **154**, A80.

138 Z. Li, Z. Zhou, G. Yun, K. Shi, X. Lv and B. Yang, *Nanoscale Res. Lett.*, 2013, **8**, 1–9.

139 L. Yang, S. Cheng, X. Ji, Y. Jiang, J. Zhou and M. Liu, *J. Mater. Chem. A*, 2014, **4**, 7338−7344.

140 S. Cheng, L. Yang, D. Chen, X. Ji, Z. j. Jiang, D. Ding, M. Liu and M., *Nano Energy*, 161−167.